AMERICAN UNIVERSITY OF BEIRUT

INVESTIGATION OF THE PHASE CHANGE PROPERTIES OF PULSED LASER DEPOSITED GERMANIUM ANTIMONY THIN FILMS

by
NOURHAN ALI BARAKAT

A thesis
submitted in partial fulfillment of the requirements
for the degree of Master of Science
to the Department of Physics
of the Faculty of Arts and Sciences
at the American University of Beirut

Beirut, Lebanon
August 2019

AMERICAN UNIVERSITY OF BEIRUT

INVESTIGATION OF THE PHASE CHANGE PROPERTIES OF PULSED LASER DEPOSITED GERMANIUM ANTIMONY THIN FILMS

by

NOURHAN ALI BARAKAT

Approved by:

Dr. Malek Tabbal, Professor — Advisor
Department of Physics

Dr. Michel Kazan, Associate Professor — Member of Committee
Department of Physics

Dr. Hassan Ghamlouche, Professor — Member of Committee
Department of Physics

Date of thesis defense: August 2, 2019

AMERICAN UNIVERSITY OF BEIRUT

THESIS, DISSERTATION, PROJECT RELEASE FORM

Student Name: Barakat Nourhan Ali
Last First Middle

◉ Master's Thesis ○ Master's Project ○ Doctoral Dissertation

☑ I authorize the American University of Beirut to: (a) reproduce hard or electronic copies of my thesis, dissertation, or project; (b) include such copies in the archives and digital repositories of the University; and (c) make freely available such copies to third parties for research or educational purposes.

☐ I authorize the American University of Beirut, to: (a) reproduce hard or electronic copies of it; (b) include such copies in the archives and digital repositories of the University; and (c) make freely available such copies to third parties for research or educational purposes after: **One ___ year from the date of submission of my thesis, dissertation or project.**
Two ___ years from the date of submission of my thesis , dissertation or project.
Three ___ years from the date of submission of my thesis , dissertation or project.

Nourha 6/9/2019
Signature Date

This form is signed when submitting the thesis, dissertation, or project to the University Libraries

Acknowledgements

I would like to express my greatest gratitude to my advisor Prof. Malek Tabbal for his guidance, motivation and continuous support at all times. Besides, I would also like to offer a very special thanks to Prof. Michel Kazan for his advice, support and help throughout these years. A special thanks to Prof. Hassan Ghamlouche for the patience, motivation and enthusiasm throughout my research. I thank you for being available at any time and ready to help me. I am truly honored and had the pleasure to work with you.

One big thank you is due to Joumana Abi Falah for her effort in making our lives easier and for advice. We appreciate all the times she listened to our nagging. Thank you Joumana for being my second mother.

I am grateful to my colleagues and friends Alaa Akouch and Kafa Alameh for all the pleasant and tough moments we've been through together during our stay at AUB. I would also like to thank all my colleagues and my roommate Zainab Fatfat who were my second family.

My sincerest love and gratitude to my family and my Alaa for their unconditional love and continuous support that they've showed throughout all these years at all times, and for all the sacrifices they've done for me to be here.

An Abstract of the Thesis of

Nourhan Ali Barakat for Master of Science
Major: Physics

Title: Investigation of the Phase Change Properties of Pulsed Laser Deposited Germanium Antimony Thin Films

Phase change materials (PCM), such as Ge, Sb and Te alloys, are materials that can switch very fast between two stable states, namely their amorphous and the crystalline phases. In addition to the interest in their physical properties, they are used in many modern technological domains such as data storage and offer great potential for non-volatile electronic memory applications. However, a good control of the stoichiometry and nanostructure of such compound materials is needed to ensure good device operation. The main goal of this thesis is to grow high quality phase change germanium antimony thin films ($Ge_{15}Sb_{85}$) by Pulsed Laser Deposition (PLD). The aim is to obtain amorphous films at room temperature with the correct chemical content that show phase change behavior. Experimental growth parameters deposition pressure, laser energy and deposition time are varied to that end. Several characterization techniques are used to determine the properties of the films: X-Ray Diffraction (XRD) to investigate the crystal structure of the films and determine their phases (amorphous or crystal), Scanning Electron Microscope (SEM) and Rutherford Back Scattering (RBS) to study the surface morphology and the composition of the films respectively. In addition, electrical measurements are performed, by measuring the sheet resistance as a function of temperature using a two probe method. The amorphous to crystalline phase transition temperature, the electrical energy gap and the behavior of the film after repeated cycles of cooling and heating are thus investigated. Optical measurements using UV-VIS-NIR spectroscopy are performed to determine the optical band gap. Finally, Raman spectroscopy measurements were also achieved to investigate the bonding in the as-deposited and annealed films.

Contents

List of Figures

List of Tables

Chapter 1

Introduction

Optical storage is any method that uses a laser to store and retrieve data from optical media. Initially, optical data storage products were only used to read the encoded information, however nowadays these products become re-writable. Two different classes of rewrite-able optical storage media have been commercialized, namely magneto-optical and phase change media [1].

The usability of phase change materials in a memory device originates from several favorable properties such as fast programming speed, low power consumption, low voltage operation, high endurance to repeated cycling, and good scalability. Phase-change materials are characterized by a unique combination of properties including fast crystallization of the amorphous phase accompanied by a drastic change of physical properties such as optical reflectance and electrical resistance. The amorphous phase is characterized by a low reflectivity and electrical conductivity, while in the crystalline phase the reflectivity and electrical conductivity are high.

Phase change materials offer great potential for emerging non-volatile electronic memories. This relies on the synthesis of alloys containing elements like Ge, Sb and Te. The relentless pursuit of material optimization and the drive to understand the underlying material characteristics have led to the development of optical storage products such as compact disks (CD), digital versatile disks (DVD), and Blu-ray disks(BD) or high-definition digital versatile disks (HD DVD), respectively [2].

In 1968, S. R. Ovshinsky first reported the phase transition phenomenon between high resistance and low resistance in $Ge_{10}Si_{12}As_{30}Te_{48}$ chalcogenide [3]. However, this phenomenon suffered from a quite slow operation speedn (of the order of microseconds) without little advantage over other storage technologies.

In 1991, Yamada et al.[4] reported a nanoseconds scale switching and sig-

nificant optical reflectivity change in $GeTe - Sb_2Te_3$ pseudobinary phase-change materials. This breakthrough enabled the successful applications of phase-change materials in rewritable compact disc (CD-RAM), rewritable digital disc (DVD), and Blue-ray disc (BD) [5]. It was found that semiconductor alloys along the $GeTe - Sb_2Te_3$ pseudobinary have large optical contrast and could be rapidly and repeatedly switched between the amorphous, low reflectivity and the crystalline, high reflectivity phases using laser pulses. This success triggered a wide the interest in PCM technology and an intense attempt has been devoted in the search of materials optimized for this technology [6].

$Ge_2Sb_2Te_5$ (GST) has been investigated most intensively due to the outstanding material properties it offers, including non-volatility, high scalability, fast programming capability, and good cyclability [7][8]. The most prominent material, $Ge_2Sb_2Te_5$ (GST), is located on the pseudobinary $GeTe - Sb_2Te_3$ tie line. It has been widely used in commercial DVD-RW. However, it is known that Te has a low melting temperature and high vapor pressure, which may lead to phase separation and reduction of reliability of the material [9]. It has also been found that Te diffusion in $Ge_2Sb_2Te_5$ could not be prevented even by capping a layer, which will result in inhomogeneity and voids in the material [10]. Furthermore, contamination of Te element in the complementary metal-oxide semiconductor manufacturing equipment is still unclear, which limits the research and development of phase change RAM as well. Hence, novel phase change materials without Te may have a good prospect in the applications of PCRAM [11][12].

In this thesis, the phase change binary compound germanium antimony ($Ge_{15}Sb_{85}$) will be grown by Pulsed Laser Deposition technique (PLD). The aim is to obtain amorphous layers with the correct chemical content at room temperature, and having phase change properties. Experimental preparation will be varied to that end. These parameters include deposition pressure, laser energy and deposition time. In addition, several characterization techniques are used to determine the nanostructure of the films: X-Ray Diffraction (XRD) to investigate the crystal structure of the films and determines their phases (amorphous or crystal), Scanning Electron Microscope (SEM) for surface morphology and the Rutherford back-scattering spectrometry (RBS) to determine the composition and the thickness of the films. In addition, electrical measurements are performed in order to deduce the phase transition temperature (amorphous– crystal), the width of that transition and the energy gap of the measure the optical band gap. Moreover, Raman measurements are carried out on as-deposited and annealed samples to investigate bonding in the films.

Chapter 2

Review of PCM and their Properties/Applications

2.1 Germanium Antimony Thin Films

The Te-free eutectic $Ge_{15}Sb_{85}$ phase change material is a promising candidate for phase change memory applications since it maintains remarkable electronic and optical contrast as required for applications. Also, it has a low melting temperature (the lowest melting temperature among GeSb family materials), which is beneficial for memory applications since it helps to decrease the power consumption during the switching. The crystallization temperature of $Ge_{15}Sb_{85}$ (512 K) is higher than that of common phase change materials like $Ge_2Sb_2Te_5$ (446 K) [13]. GeSb thin films have been prepared and characterized by many research groups. Sputter deposition is the mos commonly used technique for GeSb film growth. Eising et al. found that the activation energy for growth and the crystallization temperature increase strongly when increasing the germanium content [14]. Krebs et al. studied the electrical transport and switching in phase change materials and $Ge_{15}Sb_{85}$ was investigated. Threshold fields for several materials were investigated and it was found to be 1.8V/μm for $Ge_{15}Sb_{85}$ [15]. Wuttig and his group investigated $Ge_{15}Sb_{85}$ thin films to study the atomic structure of amorphous and crystalline phase. They noticed that the chemical stability of this composition was found to show a tendency toward phase separation into a Ge-rich and a Sb-rich phase [16][17]. Many recent papers have studied the properties of the GeSb binary materials. Byeong Geun Kim and his group [18] have deposited the binary phase change material $Ge_{1-x}Sb_x$ thin films using dc co-sputtering system in order to study their crystallization properties. They show that both the crystallization temperatures and sheet resistances of the amorphous and crystalline phases increases as the concentration of Sb in $Ge_{1-x}Sb_x$ thin films decreases and that thin films around the eutectic composition show different optical properties through their crystalline behaviors on a nanosecond scale . Work

by Yifeng Gu and his group [19] studied the variation of resistance as function of temperature for various compositions of $Ge_{1-x}Sb_x$ deposited by co-sputtering and the impact of Ge on the crystallization temperature. They also showed the different crystalline structures for the various $Ge_{1-x}Sb_x$ compositions using XRD . Furthermore, Chaochao Liu and his group [20] investigated the optical phase change properties of the intrinsic GeSb and the Ti-doped GeSb that were fabricated by the magnetron co-sputtering technique. They studied the intrinsic optical properties for both GeSb and Ti- doped GeSb through theoretical and experimental effort concluding that Ti dopant decreases the optical reflectivity and suppresses the crystallization of the GeSb film . In our work, thin films of $Ge_{15}Sb_{85}$ were deposited for the first time using the pulsed laser deposition technique. This deposition technique is attractive because of several benefits that include the stoichiometry of the target source. In previous work, thin films that have different compositions of Ge and Sb were investigated. However in our work, the main goal is the deposition of high-quality thin films in the amorphous phase having the stoichiometry of the target source (15:85) and the characterization of their properties.
Before presenting the experimental techniques used (Chapter 3) and results (Chapter 4), we shall review the basic physical principles that governs the properties of PCM.

2.2 Principle of Phase Change Materials

In a re-writable disc information is stored in the phase change memory. Phase-change materials (PCM) possess a unique property which is the fast and repeated switching between their crystalline and amorphous phases. Re-writable storage media have to be compelled to fulfill the main data storage necessities which are the following:[21]

1. Writability: Enable writing of data (easy formation of amorphous marks).
2. Archiving: Stored information has to be stable.
3. Readability: Easy to read.
4. Erasability: Information should be erasable.
5. Cyclability: Storage medium should allow numerous write/erase cycles.

In general, crystalline solids have long range order which means that there is a regular pattern of arrangement of particles that repeat itself periodically over the entire crystal. Whereas, amorphous solids consist of particles of irregular shape and have short range order only. In such an arrangement, a regular and periodically repeating pattern is observed over short distances only.

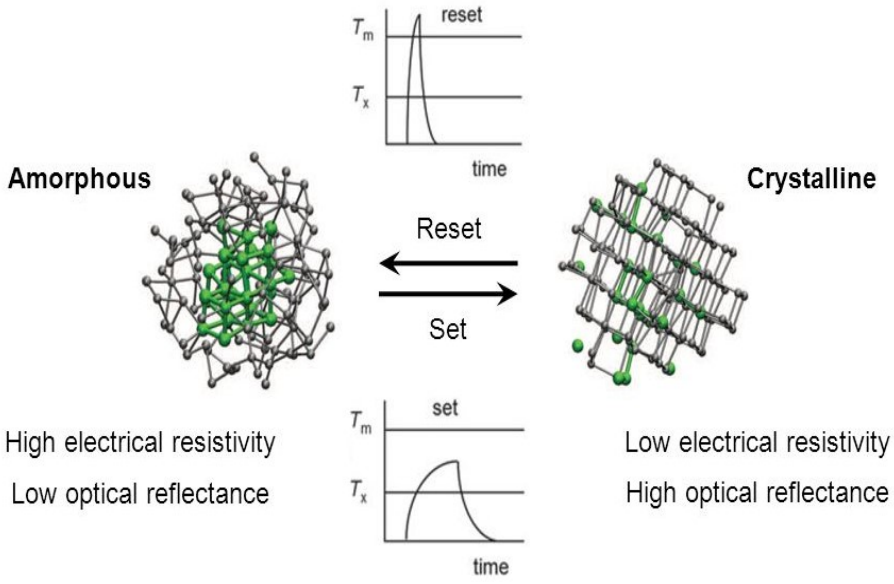

Figure 2.1: The possible transformation in the phase changes crystal– liquid – amorphous (record) and amorphous–crystal (erase).

Phase change materials possess a pronounced difference in optical and electronic properties relying on their atomic arrangement, whether or not they are amorphous or crystalline. At the same time, they can be switch rapidly between the amorphous and the crystalline states. Phase change memory is based on this switching between the two states which is the base in information storage [21].

In rewriteable optical data storage using phase change materials, an amorphous state is obtained by focusing a local high intensity laser beam on the material which actually heats it above its melting point. Then, a rapid cooling of the phase change material quenches the liquid-like state into a disordered phase called the amorphous sate. This rapid annealing process generates numerous dislocations or vacancies causing a high resistance. This is called the reset state where storing information is obtained by writing of bits which corresponds to the formation of small amorphous regions in the crystalline matrix.

On the other hand, crystallization occurs by heating the phase change film above the crystallization temperature using a laser pulse with intermediate power. At elevated temperatures above the glass transition temperature, the atoms become increasingly mobile and can revert to their favorable crystalline state. This state is also called the set state where erasure of information is obtained.
Hence, the change in the microscopic level, the atomic structure of the phase change material, is the base in storing or erasing data.

The density of states for electrons in a band yields the number of states in a certain energy range. Those states can be occupied or unoccupied by electrons and form the so-called gap. DOS is one of the most important properties of condensed materials considering electron transport and optical properties. In crystalline case where translational symmetry exist, block theorem is basically used to calculate the DOS and the results are usually displayed in inverse space (k space or reciprocal k-space), inside the first Brillouin zone of the lattice showing symmetry labels. In the electronic DOS of crystalline semiconductors there is an energy interval about 1-2 eV where we cannot find states at any k value.

As illustrated in figure 2.2, if the maximum energy of occupied and the minimum energy of unoccupied states belong to the same k than we say that this semiconductor has direct gap. In a direct band gap, the bottom of the conduction band lies directly above the top of the valence band. In Fig, the case of an indirect gap semiconductor is shown in which the bottom of the conduction band does not lie directly above the top of the valence band. In this case, the electron cannot make a direct transition from the top of the valence band to the bottom of the conduction band. Such a transition can still take place but as a two-step process. The electron absorbs both a photon and a phonon simultaneously.

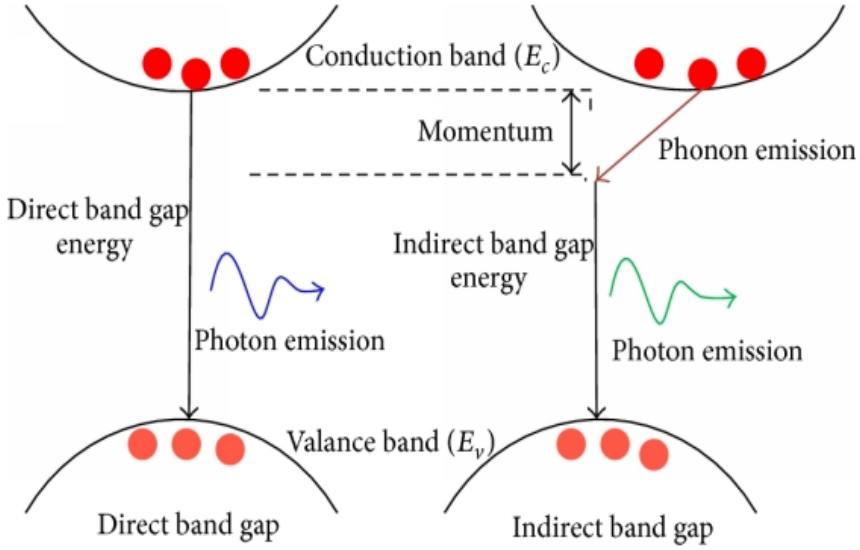

Figure 2.2: Direct and Indirect band gaps

Although crystalline semiconductors have received most attention, nevertheless there is a noticed effort toward understanding amorphous semiconductors. It is difficult to treat electron states in a very disordered solid because of the pronounced disorder rather than a periodic potential. As a consequence, the reciprocal k-space does not exist and also the Block electron theory does not work. Band

gaps do exist in amorphous materials despite the absence of long range crystalline order. However, some amorphous semiconductors show unusual switching properties that are necessary in applications like memory devices. Moreover, these semiconductors are typically cheaper to manufacture than crystalline ones that ends up in a significant reduction within the price[22].

2.3 Band Structure

In crystal semiconductors, electrons tend to fill up the low energy band which is the valence band while the higher energy band, the conduction band, is nearly empty. The difference in energies of the conduction and the valence bands form the band gap where the density of states vanishes in the range of energy gap. As shown in figure, for an amorphous semiconductor of the same substance, the density of states has extended into the gap from both the CB and the VB sides. Each of these bands has a tail (shaded region in the fig. 2.3) entirely within what was formerly a band gap.

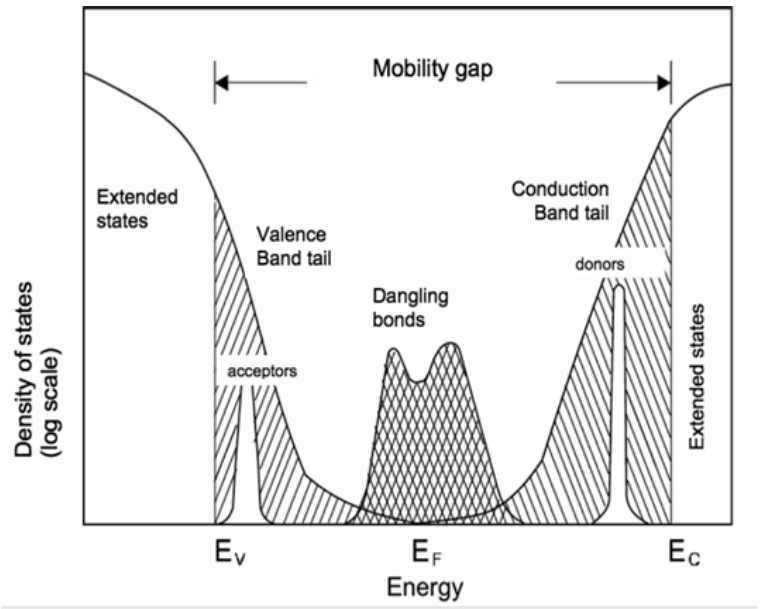

Figure 2.3: Description of the density of states in amorphous semiconductor.

Since an electron on a specific site interacts most firmly with closest neighbors, the impact of long-range disorder introduced into the crystalline state on the energy levels is fairly little (just a couple of percent). This disorder causes an up or down shift of the levels only by a small amount through the band. Near the band edge, the effect of the disorder is of great importance since it displaces

some levels right into the energy gap thus creating the band tail.

Before resuming our discussion of the density of states, we have to make a clear distinction between localized and delocalized electron states. In a localized state, the electron is restricted to movement around only one particular atomic site, while in a delocalized state the electron is extended throughout the solid (existing partly at every atomic site). In case of crystal, all states are delocalized in accordance with the Bloch theorem, while in the case of amorphous solid, both types of states occur simultaneously. The delocalized states are those in the main body of the band just as those in a crystal. One the other hand, the states in the band tail represent localized electrons[22].

The electronic density of states for a pure amorphous semiconductor is shown in figure 2.1. The non-empty gap is referred to as mobility gap (tail), and it can be found containing localized electron states that do not exist in any pure crystalline semiconductors. The rest of states around gap are delocalized and the interface between localized and delocalized states is the mobility edge.

2.4 Electronic Conduction

The most vital distinction between crystalline and amorphous semiconductors is that within the latter there is a continuous distribution of localized states among the forbidden energy gap. As illustrated in the figure 2.2, the discrete energy levels of the atom are broadened into bands of allowed energy levels separated by the energy gap. In the allowed energy band of the crystalline materials the DOS is finite while it is zero in the forbidden energy ranges. However, the DOS in amorphous can be divided into several regions. As shown in the figure, above Ec and below Ev the electron wavefunctions are extended throughout the crystal so that these states, denoted by E, are the extended states. Whereas, the states between Ec and Ev are localized states. The shaded regions, between Ec and Ea and between Eb and Ev, which are denoted by T, are due to the lack of long range order and are called the tail states. While, the states which are denoted by D arise from the defects in the material and the density of these depends critically on the method used to prepare the amorphous film.

In an amorphous semiconductor gap there is a mobility gap, defined by Ec - Ev, rather than the forbidden energy gap Eg in the crystalline DOS. Hence, the mobility gap is analogous to the band gap in ordered systems but contain the spatially localized states[23].
The idea of delocalization is vital in electronic conduction. A delocalized electron moves promptly through the solid (Section 5.3). Since electrons are distributed through the solid, they require just a little push, for instance from an electric

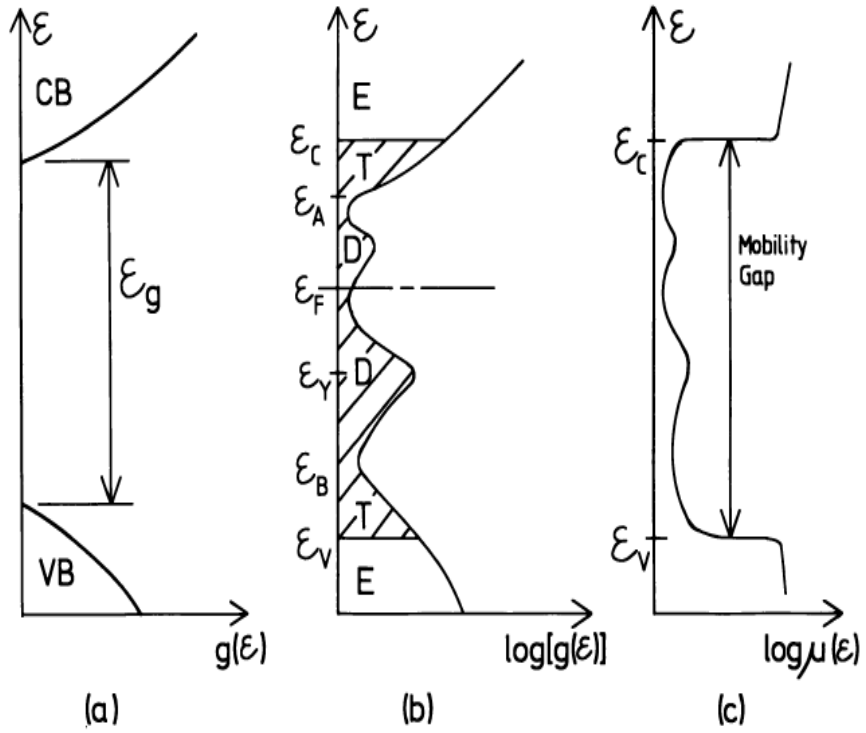

Figure 2.4: (a) Density of states function $g(\epsilon)$ in a crystalline semiconductor; CB and VB denote the conduction and valence bands respectively, (b) Density of states in an amorphous semiconductor; E, extended states; T, localized tail states; D, localized defect states, (c) The mobility as a function of energy for the amorphous sample shown in (b).

field-to set them adrift, conveying an electric current. This process is known as metallic conduction. On the other hand, a localized electron is strongly bound to its site, and isolated from the neighbors by high, thick potential barrier. Electron can move from one site to a neighboring one only if it is energetically excited above the potential barrier. But, since the barrier is usually about 1eV, relatively few electrons are excited at room temperature. This process is known as hopping, and the thermal excitation process as activation[24].

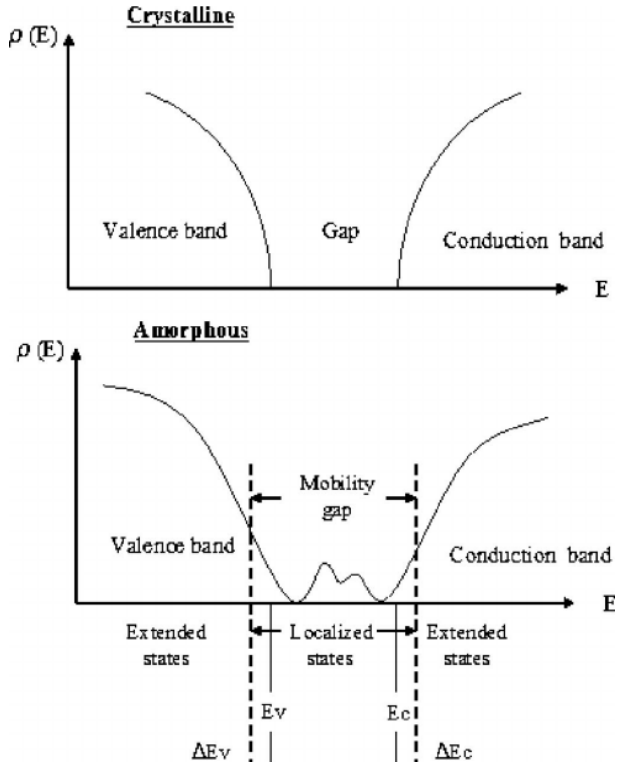

Figure 2.5: (a) The density of states versus energy E for a crystalline amorphous semiconductor. Region in middle figure represent band tails introduced by the disorder.

Figure (2.5) illustrates this graphically by plotting the mobility p of the electron as a function of the energy. For the CB the mobility drops sharply and suddenly as the energy decreases from the main band to the band tail since the mobility of a localized electron is essentially zero. A similar situation exists for the VB. So, although no sharp density-of-state gap exists, there is a sharp mobility gap, and this gap is approximately the same as the energy gap in the crystalline solid.

In order to start discussing the conduction mechanism, we must return to the form of the electron density at any particular energy, It is possible to write the electron density at any particular energy $n(E)$ in terms of the density of states at

that energy and the Fermi-Dirac probability $f(E)$ of those states being occupied.

$$n(E) = g(E)f(E) \tag{2.1}$$

where,

$$f(E) = \frac{1}{e^{(E-E_f)/K_BT} + 1} \tag{2.2}$$

where K_B is the Boltzmann constant and E_f is the Fermi energy.

Restricting ourselves to energies more than a few K_BT away from E_f, we can approximate the previous equation to the classical Maxwell-Boltzmann form, so that $n(E)$ becomes

$$n(E) = g(E) \exp \frac{-(E - E_f)}{K_BT} \tag{2.3}$$

The contribution to the conductivity from the electrons at any particular energy will the be given by:

$$\sigma(E) = e\mu(E)n(E) \tag{2.4}$$

then after plugging equation (2.3) in equation (2.4)

$$\sigma(E) = e\mu(E)g(E) \exp [-\frac{E - E_F}{K_BT}] \tag{2.5}$$

Keeping in mind that in a pure crystal, g(E) is zero within the energy gap so that $\sigma(E)$ will also be zero in this energy range. Whereas the density of states in amorphous case is finite throughout the whole energy range causing contributions in the conductivity from each of these energies. These contribution depends on g(E), $\mu(E)$and of course on the energy $E - E_f$ separating the states from E_f . Moving away from E_f , the value of $E - E_f$ becomes larger while the probability of these states being occupied by electrons get smaller (the smaller the exponential term in equation (2.5). However, The conductivity $\sigma(E)$ depends on $\mu(E)$, so this shed light on the mobility in the various energy ranges[22]. Consider the extended states illustrated in fig 2.5, the mobility of the energies well into the conduction band that is $E \gg E_c$ is similar to that of crystal. However, due to the small probability of these states to be occupied, they dont possess any significant contribution to σ.

As the energy decreases approaching E_c, the disorder within the lattice increases the scattering more, till just on top of E_c the mean free path between scattering events has attenuated from its crystalline value (of many hundred atomic distances) to a value of the order of the interatomic spacing. under these conditions the electron transport could now not be thought-about as band motion with occasional scattering, as in crystalline theory.

It has been brought up by Cohen that in this marginal area conduction is basically a diffusive process which can be viewed as Brownian motion. The electrons can be conceived as bouncing from site to site yet without the need of the thermal activation required in the typical hopping theory. This model assumes that in the conducting states of an amorphous semiconductor, the phase of the probability amplitude for finding an electron on a particular atomic site varies randomly from atom to atom and leads to the expression [25].

$$\mu(E_C) = \frac{2\pi}{3}\frac{\epsilon a^5}{\hbar} Z \frac{J^2}{K_B T} g(E_c) \tag{2.6}$$

where J is the electronic transfer integral between nearest neighbors, separated by a distance a, and z is the coordination number of the lattice under study. Taking reasonable values of the quantities, this expression leads to values of μ between 1 and 10 $cm^2V^{-1}s^{-1}$. If we refer back to equation (2.6), we notice that the mobility weakly depends on temperature. Combining (2.5) and (2.6) will lead to expression of the conduction in the extended states just above E_c.

$$\sigma(E_c) = \sigma_0(E_c) \exp\left(-\frac{E_C - E_f}{K_B T}\right) \tag{2.7}$$

where σ_0 is the conductivity pre-factor which contains the additional term involving the temperature dependence and $g(E)$. To understand the behavior of the Fermi level in the system, it is useful to start with the situation where T=0 K. At this temperature, since the donor-like trap has excess electrons, the Fermi level will be between the empty conduction band and the filled trap. When the temperature is above 150 K, the Fermi level is shifted to the middle of the band gap and carrier can be excited across the band gap. In this case the activation energy EA is approximately half of the band gap since it is the difference between the Fermi level and the conduction band. Equation (2.7) can thus be expressed as

$$\sigma = \sigma_0 \exp\left(-\frac{E_g}{2K_B T}\right) \tag{2.8}$$

2.5 Hopping Conductivity

The transition from extended to localized states is of essential significance in the understanding of conductivity in the amorphous materials. The states between Ec and Ev which include tail states and defect states are localized, this leads to the fact that the transport process will not be the same as in the extended states above Ec or below Ev. This transition from extended to localized states is essential in understanding the conductivity in amorphous materials. The nature of transport in these states is the hopping process.

The case explained above deals with nearest neighbor hopping. However, Mott [26] proposed that at low temperature rather than hopping a distance R to the nearest site for which the electron gains an energy W from the lattice (as shown in figure (2.6), it is favorable that the electron will hop a longer distance if this process involves a smaller energy jump.
The process has been called variable range hopping at low temperatures, we are choosing to hop a larger distance R in favor of a smaller energy W [27].

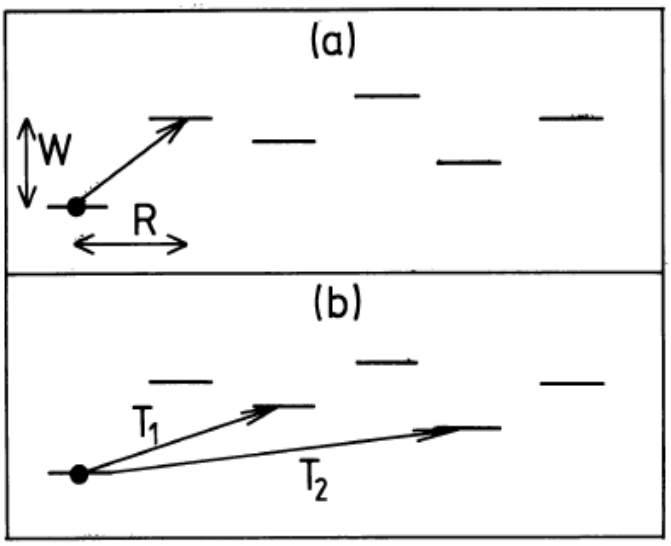

Figure 2.6: Hopping between localized states: (a) nearest neighbor hopping, (b) variable range hopping at lower temperatures T_{21}

2.6 Optical Properties

The optical properties of a semiconductor can be defined as any property that involves the interaction between electromagnetic radiation or light and the semiconductor, including absorption, diffraction, polarization, reflection, refraction, and scattering effects. The electromagnetic spectrum is an important vehicle for giving an overview of the types of measurements and physical processes characteristic of various regions of interest involving the optical properties of semiconductors. Most optical properties of semiconductors are integrally related to the particular nature of their electronic band structures. Their electronic band structures are in turn related to the type of atomic structure. In order to obtain information about optical properties of the film under investigation the absorption phenomenon is studied. The most general and characteristic property of semiconductors is the gap in their electronic density of states between the valence and

conduction bands. Optical absorption is a standard technique for investigating band structure, and it is therefore of interest to study absorption in semiconductors. In fundamental absorption, an electron absorbs a photon and jumps from the valence band to the conduction band. The photon energy must be equal to the energy gap, or larger. In the transition process, the total energy and momentum of the electron-photon system must be conserved. The absorption coefficient α of a material is defined by the relation

$$I = I_0 \exp -\alpha x \tag{2.9}$$

If light of initial intensity I_0 propagates a distance x in the material, its intensity decreases from I_0 to I . (Note that the initial intensity of the light within the medium is the intensity of the fraction of the light that is incident upon the layer in question that is not reflected or scattered at its surface).The value of α is related to the optical constant k by the expression

$$\alpha = 4\pi K/\lambda \tag{2.10}$$

Where λ is the wavelength of incident light. The measurement of α as a function of wavelength for a semiconducting material (its optical absorption spectrum) is a very important and widely applied method of measuring the materials energy band gap and several other features of the band structure [28].

2.6.1 Absorption Processes

Optical absorption is a standard technique for investigating band structure, and it is therefore of interest to study absorption in semiconductors. In semiconductors, a number of distinct optical electronic processes take place independently. However, the most important absorption process involves the transition of electrons from the valence band to the conduction band. This process is referred to as fundamental absorption. In fundamental absorption, the electron absorbs a photon (from the incident beam) and jumps from the valence band to the conduction band. For this to occur, the photon energy must be equal to the energy gap or larger. . In the transition process, the total energy and momentum of the electron-photon system must be conserved.

As mentioned in section (2.3), when the bottom of the conduction band lies directly above the top of the valence band, the absorption process occurs in the direct-gap semiconductors (figure 2.4). In this case, the absorption coefficient has the form [22]

$$\alpha h\nu = \beta(h\nu - E_g)^{\frac{1}{2}} \tag{2.11}$$

where α is the absorption coefficient, $h\nu$ is the photon energy, β is a constant involving the properties of the band. However, there are also indirect-gap semiconductors (figure 2.5), in which the bottom of the conduction band does not

lie directly above the top of the valence band. In this case, the electron cannot make a direct transition from the top of the valence band to the bottom of the conduction band. Such a transition can still take place but as a two-step process. The electron absorbs both a photon and a phonon. The photon supplies the needed energy, while the phonon supplies the required momentum.

In 1968, Blatt made the Calculation of the indirect-gap absorption coefficient and the following formula was derived [15]:

$$\alpha h\nu = A(T)(h\nu - E_g)^2 \tag{2.12}$$

Where A(T) is a constant involving the properties of the band and is temperature dependent due to the phonon contribution to the process. The plot of α versus the photon energy $h\nu$ gives the optical energy gap from the linear extrapolation of the curve. We may also use this optical method to distinguish between direct and indirect-gap semiconductors.

2.6.2 Tauc Plot

Tauc plot is a mathematical plot used plot $(\alpha h\nu)^{\frac{1}{r}}$ versus the energy of the photon $h\nu$ where α is the absorption coefficient of the material and is the absorption divided by thickness of the thin film under study. This plot is used to determine the energy band gap of the material. Also it gives the type of the band gap whether it is direct, indirect or forbidden band gap. The type of the band gap can be determined from the r value. For $r = \frac{1}{2}$ then the transition is a direct allowed transition whereas for $r = 2$ the transition is an indirect allowed transition. To calculate the band gap of the sample a linear line must be obtained from the plot. If there is no linear line, then the type of the band gap is not true and we have to change the value of r in order to obtain the correct type as we obtain a straight line we extrapolate the linear region to the abscissa and this intersection gives the band gap of the material under investigation. The band gap is determined by the intersection of the linear part of the graph by the abscissa coordinate.

Chapter 3

Experimental Techniques and Procedures

3.1 Introduction

In this chapter we described the Pulsed Laser Deposition system used to grow germanium antimony $Ge_{15}Sb_{85}$ thin films and the different characterization techniques used to characterize their properties, namely:

- X-Ray Diffraction (XRD)
- Scanning Electron Microscopy (SEM)
- Energy-Dispersive X-Ray Spectroscopy (EDX)
- UV-VIS NIR Spectroscopy
- Rutherford back-scattering spectrometer (RBS)
- Resistance versus temperature measurement
- Raman Spectroscopy

3.2 PLD Experimental Setup

The PLD workstation setup used consists of a high vacuum deposition chamber that can be pumped down to 10^{-7} mbar by a turbo-molecular backed by diaphragm pumps. The chamber consists of a substrate holder and a target manipulator that can hold up to four different targets. The substrate holder is placed directly above the target and has a shutter. Both the target and the substrate holder are connected to rotary drives to allow their rotation. The control panel is used for the adjustment of the pressure and the flow of argon gas.

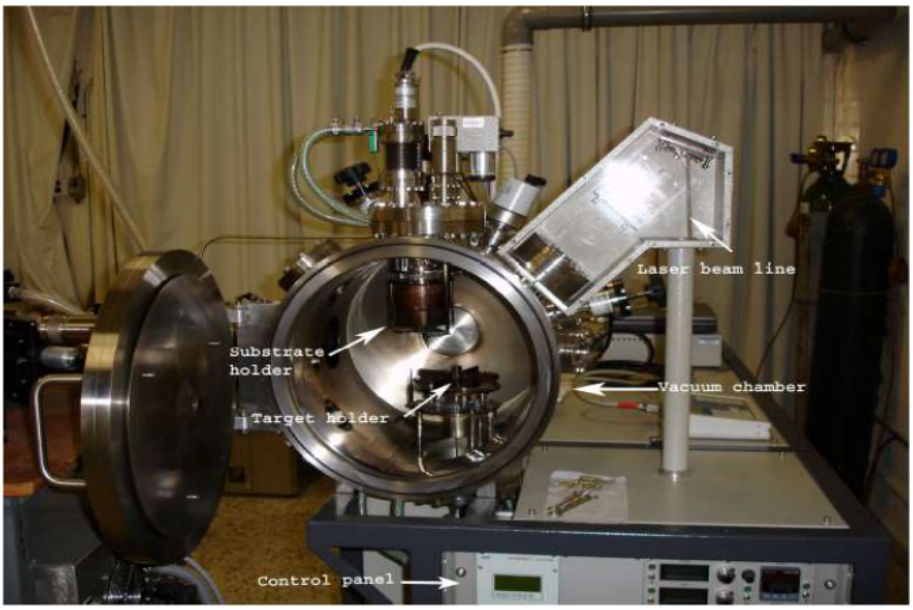

Figure 3.1: Pulsed Laser Deposition (PLD) setup

The laser used is a KrF excimer laser operating at 248 nm wavelength, 20 ns pulse duration with an adjustable repetition rate or frequency (1-50 Hz) and laser energy up to 700 mJ. A beam-line consisting of two mirrors and a lens guides and focuses the laser pulses on the target. Due to the energy of the laser pulses, atoms will be ablated from the surface of the target in the form of a plasma plume, reaches the substrate and are deposited on it and forms the desired film. The growth of the GeSb films was achieved as follows: The laser was allowed to warm up for 8 minutes before being used. After cleaning the chamber, the substrates were glued to a 2 inch round metal plate using carbon paste. The GeSb target, metal plate and substrate holder were installed in their position in the PLD chamber which was then cleaned and wiped with alcohol (isopropanol, ethanol or methanol), dried with N_2 gas and put under vacuum. After reaching vacuum argon gas was introduced into the chamber to attain the required pressure. Sometimes the rotational speed of the pump was adjusted in process of achieving the required pressure. Before starting our deposition, the GeSb target was cleaned by shooting it by the laser for five minutes whose high voltage was set at 20 kV and repetition rate 10 Hz. Finally, it is time for deposition. The substrate-target distance is set, the energy mode is chosen from the laser controller (energy mode, no gas refill EGY NGR), and the laser energy, and repetition rate are selected. After deposition, argon input was disabled, and the sample was removed from the chamber.

3.3 Characterization Techniques and Analysis of Thin Films

3.3.1 X-Ray Diffraction (XRD)

X-ray diffraction investigates the crystal with x-ray radiation having a wavelength close to the crystal lattice spacing. Constructive and destructive interference and diffraction phenomena should be observed when a crystal or molecular structure is exposed to x-rays because the interplanar distances and wavelength of x-rays are comparable. X-rays are generated by bombarding a metal with electrons in an evacuated tube and monochromatic x-rays are usually selected. These x-rays are scattered by the electron cloud surrounding each atom in the crystal. A crystal can be viewed as a set of lattice planes separated by a distance; in which hkl are the Miller indices that defines the lattice planes. In x-ray diffraction, the sample is illuminated by x-rays that impinge them at an angle θ [29]. The incident angle θ is varied leading to a variation in the intensity of the reflected waves. Constructive interference occurs between the scattered x-rays when the path difference AB ($n\lambda$) is equivalent to $2d\sin\theta$. This is the basis of Braggs law, which relates the spacing between the planes of atoms from which diffraction is occurring (d) to the angle (θ) at which the incident monochromatic beam must probe the plane to give constructive interference:

$$n\lambda = 2d\sin\theta. \tag{3.1}$$

This is geometrically visualized in figure (3.2):

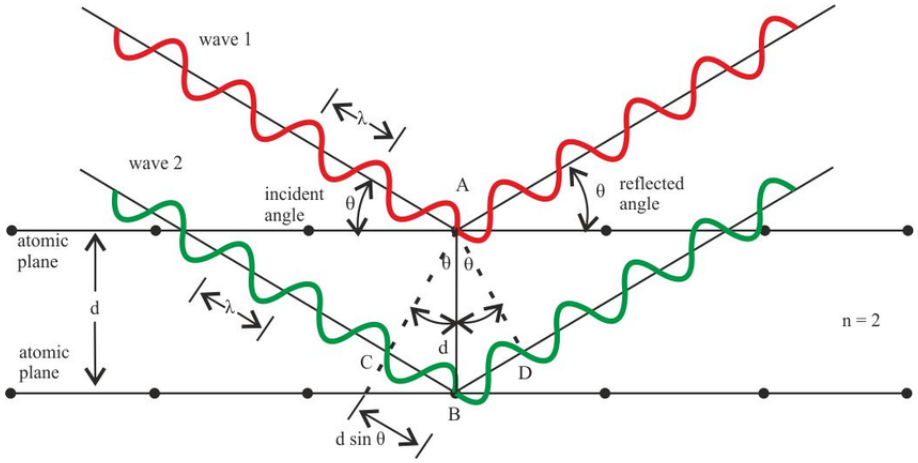

Figure 3.2: Bragg's law geometry

There are two different geometries that we used in XRD which are the Grazing Incidence and the Bragg-Brentano ($\theta/2\theta$) geometries. Grazing incidence x-ray diffraction (GIXRD) and the Bragg-Brentano (BB) are two method used in thin film analysis. Diffraction can be illustrated in the context of the reciprocal lattice. If the incident (k_0) and diffracted (k_h) beam vectors make appropriate angles with respect to the crystal, the scattering vector (Q, equal to (k_h) − (k_0)) will end at a reciprocal lattice point. It should be noted that Q also represents the position of the detector.

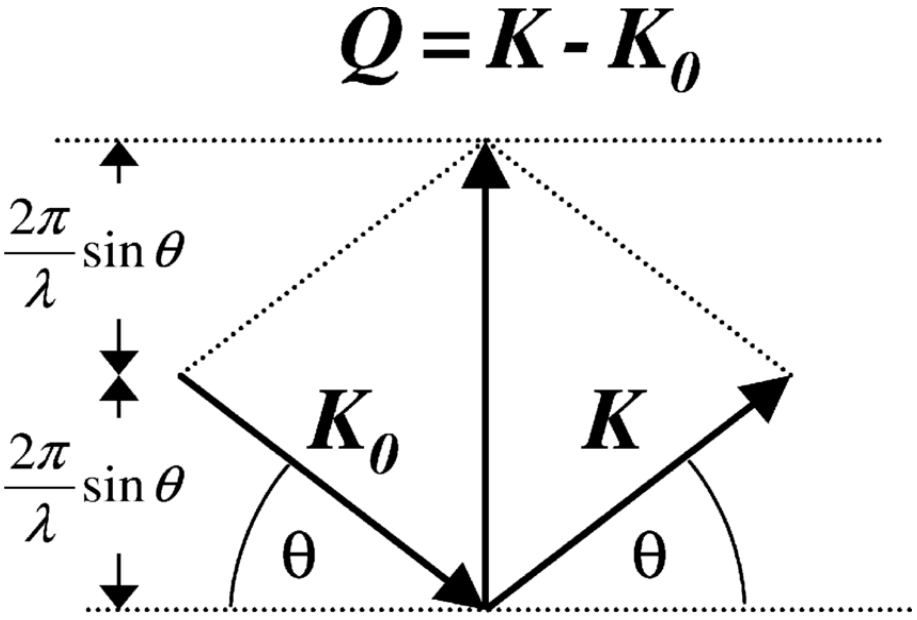

Figure 3.3: Geometry of scattering vector construction

In the BB geometry, the XRD scan type is named locked coupled or $\theta/2\theta$, the x-ray beam is incident on the sample at a variable angle θ and the detector scans at the same angle. During the scan both the angle of the incident and the outgoing beams are continuously varied, but are equal at all times. In this geometry, the scattering vector Q has a fixed direction; it is always perpendicular to the surface of the sample, so only the planes that are parallel to the surface and perpendicular to Q will contribute to a peak in the XRD pattern [29]. The reason for naming the scan $\theta/2\theta$ is because the variation in the exit variable angle (2θ) is coupled the incident one (θ).
In GIXRD, the incident beam of x-rays is held at a fixed and small angle θ (θ =1°, 2° or 3°), while the detector scans a certain angular range (2θ). Hence it should be emphasized that in this configuration the scattering vector Q changes both its magnitude and direction.

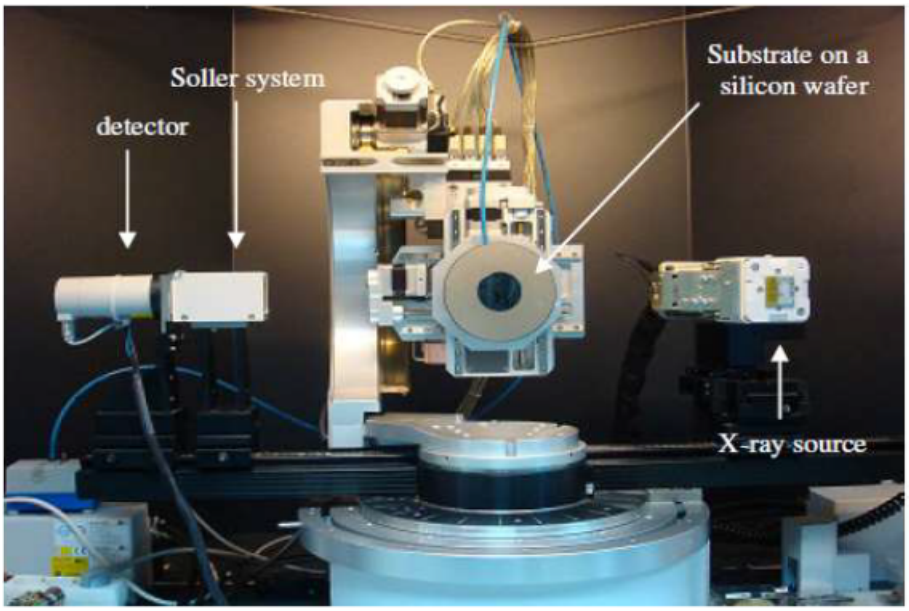

Figure 3.4: Bruker AXS D8 Discover X-ray diffractometer used

The X-ray measurements were performed using fully automated D8 Discover. In the D8 Discover Bruker diffractometer, the X-ray source consists of a ceramic Siemens tube operating at 40 kV with a current of 40 mA and emitting a $CuK\alpha$ radiation of wavelength $\lambda = 1.5418\mathring{A}$. The diverging x-rays emitted from the x-ray tube are transformed into an intense parallel beam by a Gbel mirror (Bruker AXS XRD user's manual, 2010), which is free of K_{beta} radiation eliminated by placing a nickel (Ni) filter. A soler slit placed between the sample and the detector collimates the diffracted beam. The parameters chosen for x-ray measurements of all samples are 0.2 s as the time per step, 0.02° as the increment and 5°-90° for the (2θ) range. The collected data and patterns were then analyzed by Bruker EVA software.

3.3.2 Scanning Electron Microscopy (SEM)

The development of the secondary electron microscopy started in 1926 and has proved to be a powerful tool for characterizing the shape and the size of nanostructures. It requires an electron optical system to produce an electron probe, a specimen stage to place the specimen, a secondary-electron detector to collect secondary electrons, an image display unit, and an operation system to perform various operations. SEM scans a focused electron beam from an electron gun across the sample. Then a condenser lens, which is placed below the electron gun, adjusts the diameter of the electron beam and a focused electron beam is produced. The specimen stage performs the horizontal (X, Y) movements, the

vertical (Z) movement and the rotation (R). The X and Y movements are used for the selection of a field of view while the Z movement provides the change of the image resolution and the depth of focus. Finally, the secondary electron detector is used for detecting the secondary electrons emitted from the specimen. A scintillator (fluorescent substance) is coated on the top of the detector and a high voltage around 20 KV is applied. The secondary electrons are attracted to this voltage and a light is generated as they hit the scintillator. The light is directed to a photo-multiplier tube through a light guide. Then, the light is converted to electrons which are amplified as an electric signal by a signal amplifier. These amplified signals modulate the brightness of each spot in a two or a three dimensional picture which is displayed on a cathode ray tube (CRT). Hence, every spot on the CRT corresponds to a spot on the surface of the sample. The brightness of a certain area in a SEM image is a measure of the intensity of the secondary electrons detected; the surface areas directly facing the detector will appear bright, while holes and cavities will be pictured as dark areas[30].

The MIRA 3 series scanning electron microscope, which is available in the CRSL, was utilized for imaging the surface of our thin films. It is a family of fully PC controlled scanning electron microscopes equipped with a Schottky Field emission electron gun designed for high vacuum or variable pressure operations.

The sample was installed in the SEM chamber that was then evacuated by pumping it. The high voltage was set at 20 kV. At first, for each scan auto gun centering was applied, in order to obtain high quality images. The basic SE (secondary electron) detector was chosen and the resolution mode was selected to take topographic images of our samples. Next, the magnification and the working distance (WD), which is the distance where the electron beam focuses, were adjusted to get a clear image after which the working distance and the Z position of the sample stage (WD and Z) was lowered to get a more resolved image. Further enhancement of the image was done by adjusting WD and Z with small increments and the stigmators, in addition to centering the column manually. By selecting manual column centering the image starts wobbling, periodically changing its working distance, and to achieve a clear image we had to manually minimize the movement of the image by the trackball on the Pad panel. The manual column centering is suitable for high magnification images.

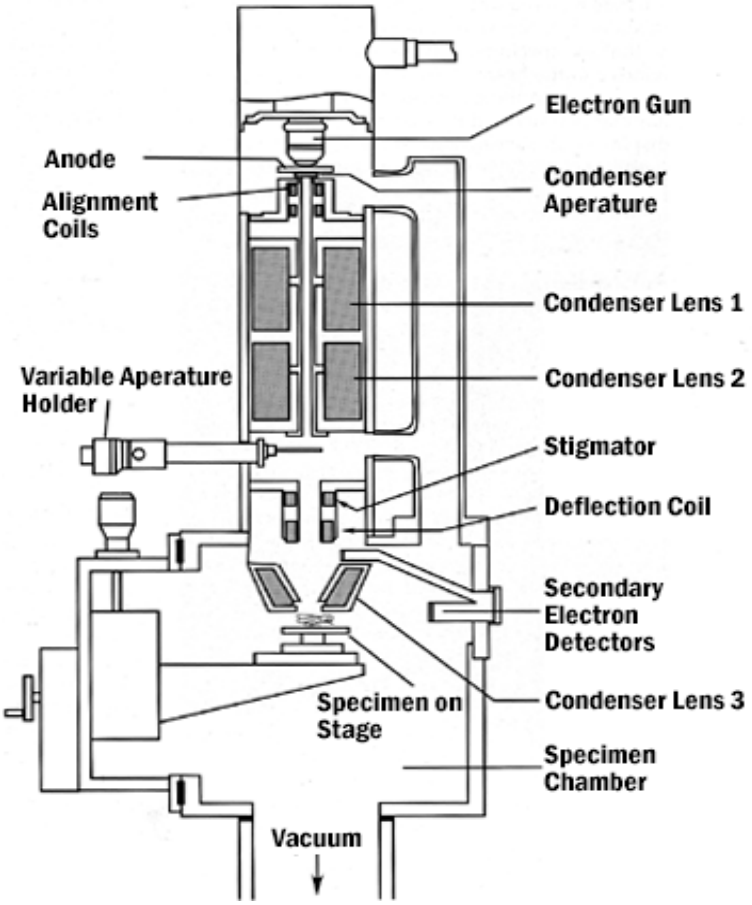

Figure 3.5: Cross sectional representation of the optical elements of the SEM

3.3.3 Energy-Dispersive X-Ray Spectroscopy (EDS)

The X-ray energy dispersive micro-analyzer is always coupled to a scanning electron microscopy (SEM). It is an analytical technique that identifies the chemical composition of the sample. It depends on the X-ray generated by an accelerated electron beam striking the surface of the sample. A high-energy beam of electrons is focused into the atoms of the sample being studied electron in an inner shell of the atom is excited and with high enough energy the electron in this shell will be expelled creating a hole in its place. The hole will be filled by an electron from a higher energy shell. This transition will emit a photon in the form of X-rays. Since the energy dispersive spectrometer monitors the number and energy of x-rays emitted from the sample the energy of these emitted x-rays is linked to the difference in energy between the higher and the lower shells i.e. to the atomic structure, the chemical composition of the sample is determined. As the energies of the X-rays are characteristic of the difference in energy between the two shells and of the atomic structure of the emitting element, EDS allows the elemental composition of the specimen to be measured.

In order to study the elemental composition of the targeted sample, we use the INCA energy system. This system consists of a PC loaded with INCA energy software, an x-stream module to control x-ray acquisition and an EDS detector to detect x-rays. Before turning the INCA energy system on and start acquisition of the data the LED of the SEM system has to be turned on and the working distance (WD & Z) has to be set at 15 mm inorder not to damage the system. INCA allows data and spectrum acquisition of different regions selected by the user.

3.3.4 UV-VIS NIR Spectroscopy

The UV-VIS spectroscopy technique is an optical characterization technique that uses ultraviolet, visible and sometimes near infrared (NIR) radiation to study electronic transitions between the atomic and molecular energy levels. UV-VIS spectroscopy deals with the interaction of electronic radiation with matter involving the measurement and the interpretation of absorption or emission of electromagnetic radiation. It can be referred to as either absorption or reflectance spectroscopy in the UV-VIS-NIR spectral range.

This technique has proven to be an efficient technique in determining the band gap of the sample under study. We have chosen absorbance spectroscopy which involves the measuring of the absorption of the radiation energy that is photons, as a function of the wavelength due to its interaction with the sample. The electron will absorb photon and jumps from the valence band to the con-

duction band. This photon energy is equal to the energy bad gap of the sample under study.

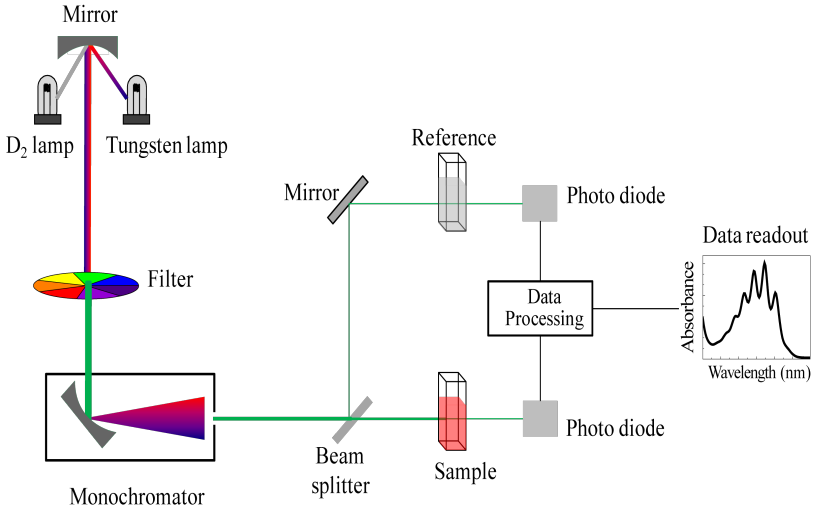

Figure 3.6: Schematic representation of the UV-VIS NIR spectroscopy used

UV-VIS NIR absorption measurements were done using a UV-VIS spectrometer which is found in the CRSL lab. It enables us to measure in a broad wavelength from 200 nm to 2000 nm which is in the ultraviolet, visible and near infrared regions and can be referred to as UV-VIS-NIR spectroscopy. This spectrometer allows us to measure the absorbance, transmittance, absolute and relative reflectance.

A beam of light from the light source is separated into component wavelength by a diffracting grating. This beam is split into two equally radiated beams by a chapper. One beam passes through the thin film sample and the other beam passes through the reference which is the glass substrate. The intensities of the light beams are measured by detectors and compared. If the intensity of the reference beam is I_0 and that of the sample is I then if the sample absorbs light then I is less than I_0 and the absorbance (abs=log I_0/I) is plotted versus the wavelength.

3.3.5 Rutherford Back-scattering Spectrometer (RBS)

Rutherford backscattering spectroscopy is a nondestructive nuclear method used for the study of thin layers and multilayer systems with thickness from nm to m. It

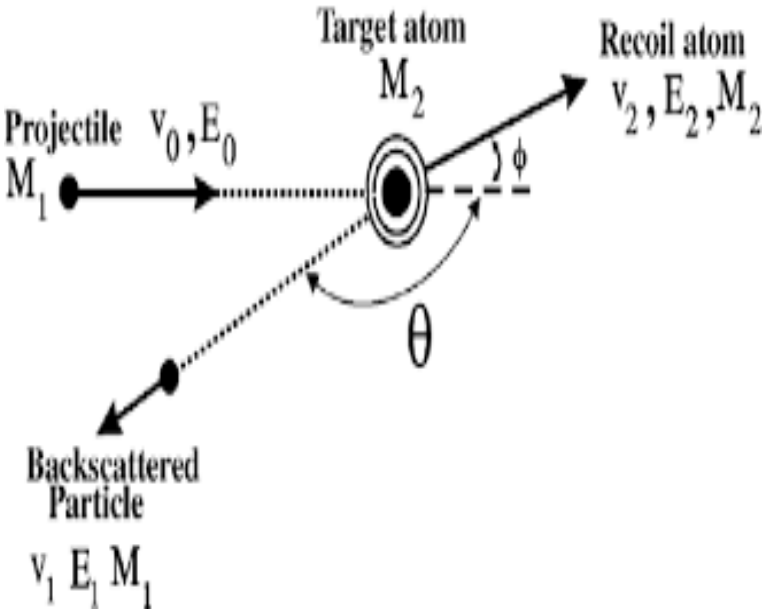

Figure 3.7: Scattering of moving ion (M1) of energy $E_0 by the target atom (M2)$

allows us to determine the atomic mass, the concentration of the elemental sample and the depth profiling of individual elements. It also has a good depth resolution of the order of several nm, and a very good sensitivity for heavy elements of the order of parts-per-million (ppm). The measurements of RBS can be performed on amorphous as well as crystalline materials. It involves measurement of the numbers and energy distribution of energetic ions (usually MeV light ions such He+) backscattered from atoms within the near-surface region of solid targets. Ions for RBS are usually light ions (H+, He+) with energy units MeV. However, the hitch of the RBS is its low sensitivity for the light elements. The sample is bombarded with light ions (H+ or He+ ions) and usually in the MeV ranges (0.54 MeV). An energy sensitive detector which is solid state detector records the energy of the backscattered projectiles. The basic principle is contained in the kinematics for binary collisions. A beam of known particles (ions) with mass M1 is given the energy E0 and directed onto the sample containing the particles M2 that are under study. The energy E1 and the scattering angle of the particle M1 are detected. From the conservation laws of energy and momentum, it is then possible to deduce the mass of the target particles M2 . Moreover, since the probability of scattering in a certain angle is known by the so called Rutherford cross section, it is also possible to estimate the abundance of M2 particles in the sample by counting the yield of scattered particles M1 in a certain solid angle covered by the detector. A typical Rutherford backscattering setup consists of a particle accelerator that can deliver beams of low-mass ions in the MeV range. In CNRS, a tandem accelerator is used. This machine produces negative ions that are accelerated towards positive potential. The particles are transported

in a vacuum system and at the high voltage terminal electrons are stripped off and the particle charge becomes positive. Then they are repelled by the high positive voltage and increase their energy further. The beam is then analyzed and directed to the target chamber. The beam diameter is about a millimeter at the target.
In our study, RBS technique was used to detect the film composition and its thickness. The GeSb sample was bombarded with alpha particles at the energy of 3 MeV and the data was collected using SIMNRA code.

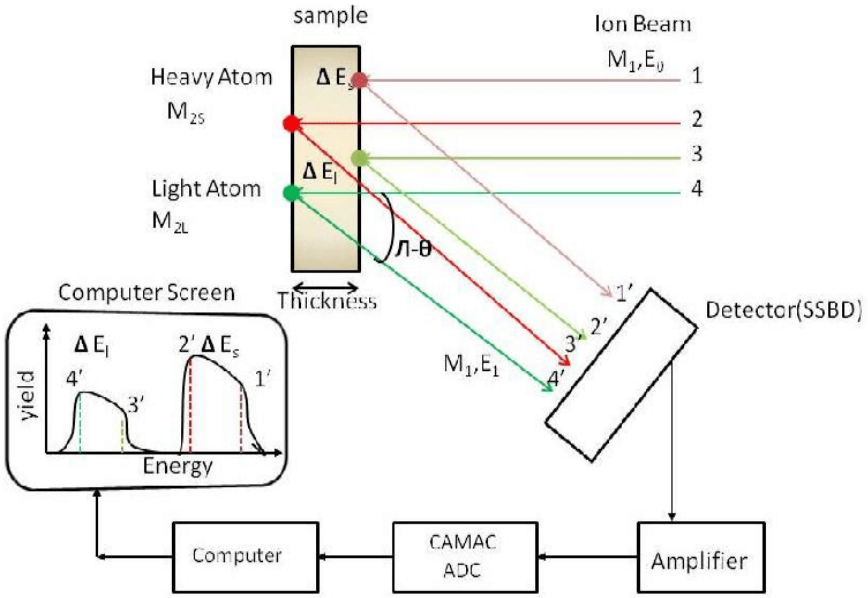

Figure 3.8: Typical ion beam scattering setup in backscattering configuration

3.3.6 Resistance versus Temperature Measurement

The resistance versus temperature measurements is the electrical technique used to determine the energy band gap of the thin film under study. The obtained thin film is cut into rectangular pieces. One of the pieces is pasted on a block using silver paint. The block is placed on a heating plate, and a thermocouple is connected to both the block and a multimeter to read the temperature. Another multimeter is used to read the resistance of the film. Two parallel lines of silver paint will be put on the sample in order to stick the two wires connected to the mutimeter. As the sample is heating gradually we record the resistance versus temperature. The measurement of the resistance versus time enables us to determine the transition temperature of the thin films and the electrical energy gap. After obtaining the measurements, the plot of the curve of ln(R) versus 1000/T is drawn. The transition temperature and the energy gap are obtained

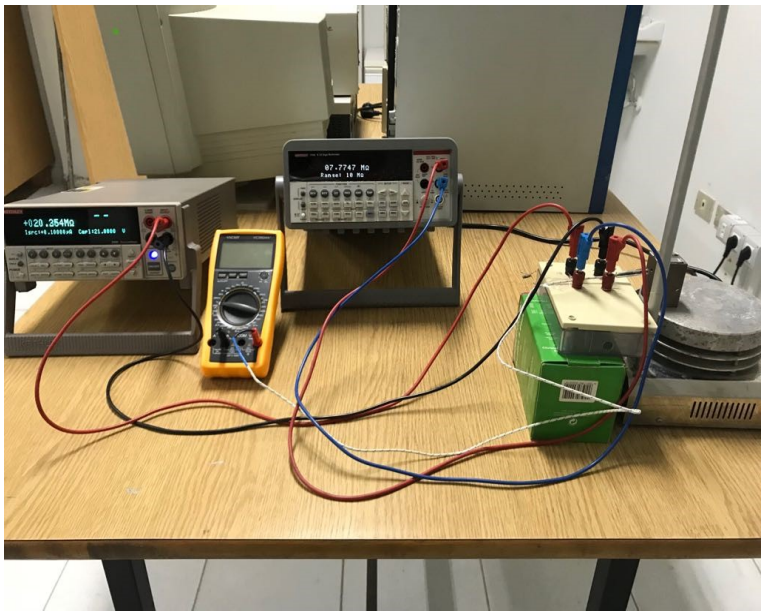

Figure 3.9: The setup used to measure resistance versus temperature using two probe method.

from the slope of the graph.
In our case, two probe methods were used knowing that the four point probe is usually preferable over the two-point probe. In a four point probe, one can obtain an accurate calculation of the resistivity due to the very little contact and the spreading resistance associated with the voltage probes. However in our case we want to determine the relative behavior of resistance and not the actual value of resistivity so we used the two probes method.

3.3.7 Raman Spectroscopy

Raman Spectroscopy is a non-destructive technique which provides information about the chemical structure, crystallinity and molecular interactions. It is based on the interaction of light with the chemical bonds within a material. Raman spectroscopy studies the vibrational characteristics of molecules, where The general spectrum profile provides a unique chemical fingerprint that can be used to identify a material, and distinguish it from others. Monochromatic light, usually from a laser, is used to illuminate a sample. Inelastic or Raman scattering occurs when a photon interacts with functional groups of the sample molecules. The majority of energy shifted photons are to a lower energy state that corresponds to the vibrational energy mode of the functional group that caused the shift in the first place. The Raman spectrometer is an optical instrument for measuring the intensity of light relative to Raman shift from the wavelength of the exciting laser. Scattered light is collected from the sample and enters the device through

the aperture and is separated into its component wavelengths by a holographic grating. The separated light is then focused onto a CCD array detector where the intensity of each wavelength is then measured by a pixel of the array. The CCD is then read-off to a computer and the result is a spectrum which displays the intensity scattered light as a function of wavenumber from the exciting laser line. Raman spectroscopy technique was used in our work to determine the difference between the as-deposited and annealed samples. The spectra obtained allowed us to determine the molecular bonds and the crystilinity of the studied GeSb films.

Chapter 4

Results and Discussion

The quality of the deposited GeSb films using PLD technique is affected by several deposition parameters. The main parameters are laser energy, deposition pressure and deposition time. In this chapter, we discuss the effect of those parameters on the structural, morphological, electrical and optical properties of the films using the characterization techniques mentioned in chapter 3. Deposition conditions for the grown samples are listed in Appendix A.

4.1 Characteristics of the Target

Figure 4.1 shows the XRD signal of the GeSb target. The XRD signal of the target shows diffraction peaks at several angles.These angles correspond to different lattice planes of A7 rhombohedral crystal structure, respectively.

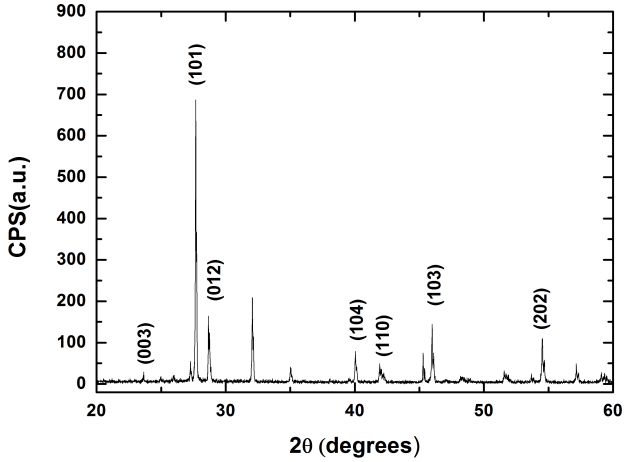

Figure 4.1: XRD spectrum of the $Ge_{15}Sb_{85}$ target

4.2 Structural Characteristics

4.2.1 Effect of Laser Energy

Figure 4.2 shows the XRD patterns of GeSb thin films at 350 mJ, 300 mJ, 200 mJ, 130 mJ and 100 mJ. No diffraction peaks is observed in 300 mJ, 200 mJ, 130 mJ and 100 mJ. When the laser's energy is 350 mJ a diffraction peak is observed at 28° which corresponds to (012) lattice plane. Hence, crystallization of the deposited thin films starts to appear at energy 350 mJ. The broad peak at 30° found in all the samples is from the glass substrate.

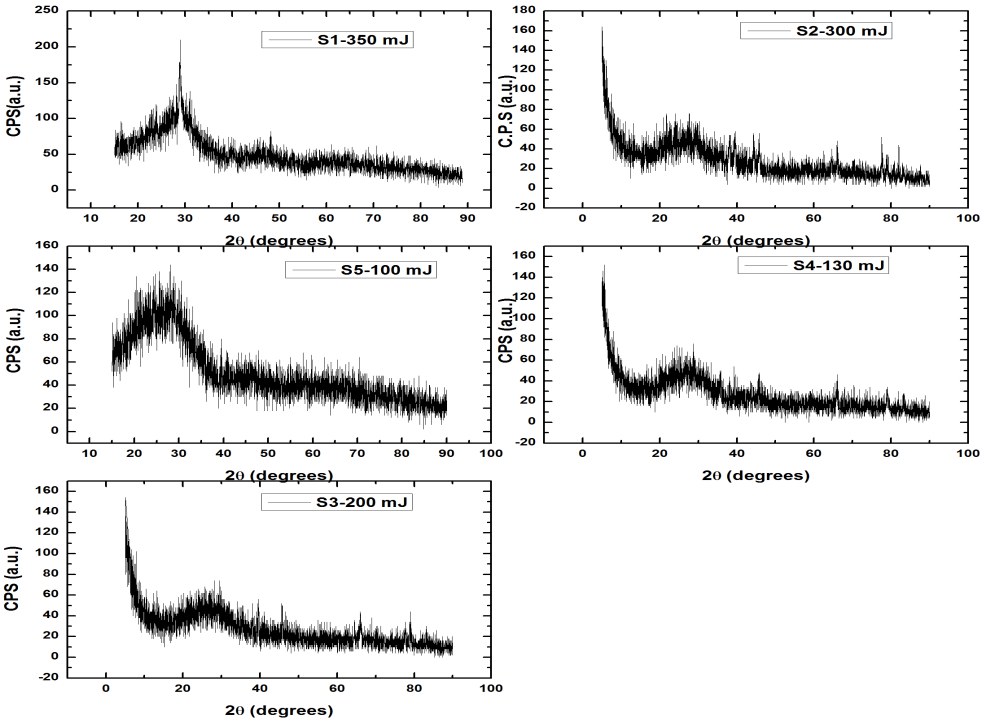

Figure 4.2: XRD spectra of GeSb samples at different energies 350 mJ, 300 mJ, 200 mJ, 130 mJ and 100 mJ respectively.

Figure 4.3 shows the SEM images for the films deposited at different laser energies. All films are crack free and appear smooth except for the existence of droplets. Films prepared at low laser energy (S4 and S5) have less droplets, while those prepared at higher laser energy contain particulates and clusters in sub-micro size. The formation of the clusters or irregular shape particles can be explained by laser splashing. Splashing is the ejection of micron-sized particulates or macroscopic particulates throughout the ablation process; three reasons for its occurrence are subsurface boiling, recoil ejection and exfoliation. Briefly, subsurface boiling is the superheating of the subsurface layer before surface material is ablated hence the boiling subsurface materials are ejected as micron-sized globules, recoil ejection is also termed shock-wave-induced droplet expulsion, and it is caused by the recoil force or pressure exerted by the plasma plume; the ejected particulates are in the submicron range. Lastly, exfoliation is a morphological process; the material ablated leaves on the target surface deep areas creating outgrowth microstructures around which are mechanically weak and are thermally decoupled and broken away upon two or more laser shots [31]. It is clearly noticed from SEM images that film prepared at energy of 100mJ has good surface morphology. Further increase of the laser energy leads to an increase in the density of the clusters and droplets on the grown films.

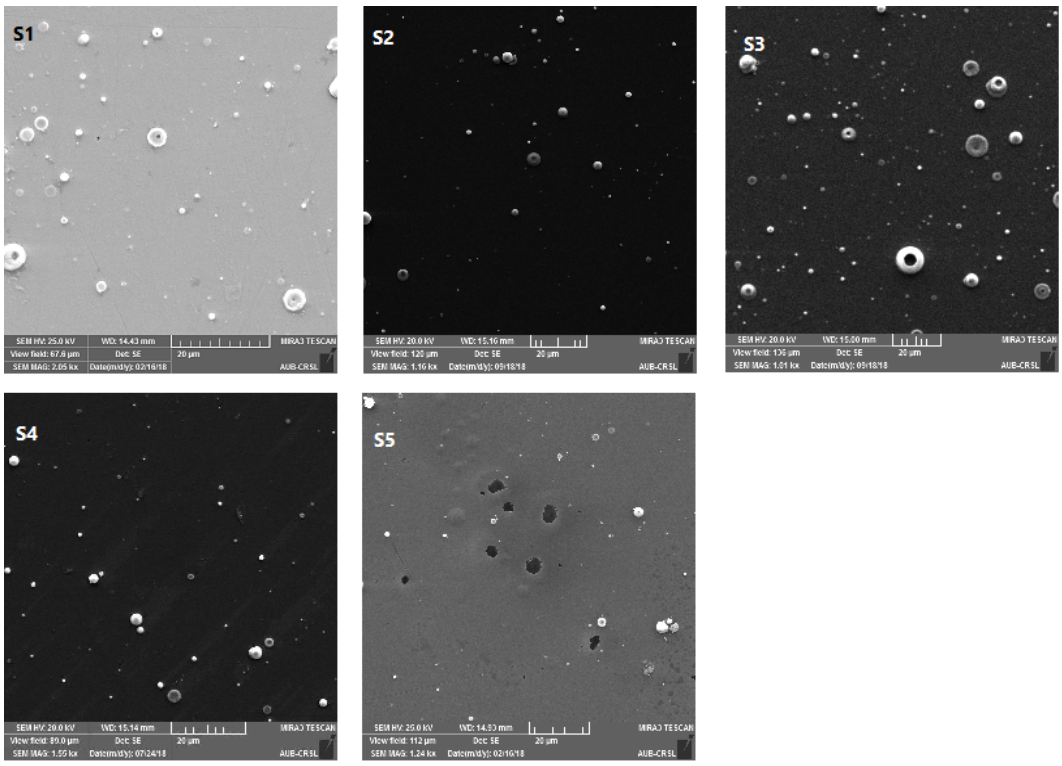

Figure 4.3: SEM images of GeSb films deposited at (S1) 350 mJ, (S2) 300 mJ,(S3) 200 mJ,(S4) 130 mJ and (S5) 100 mJ respectively

The elemental composition, stoichiometry, and thickness of the deposited GeSb thin films were determined using RBS technique, (uncertainty on the measurements ≈1%). The SIMNRA code was used to fit the simulation over experimental data and give information regarding the stoichiometry and the concentration.

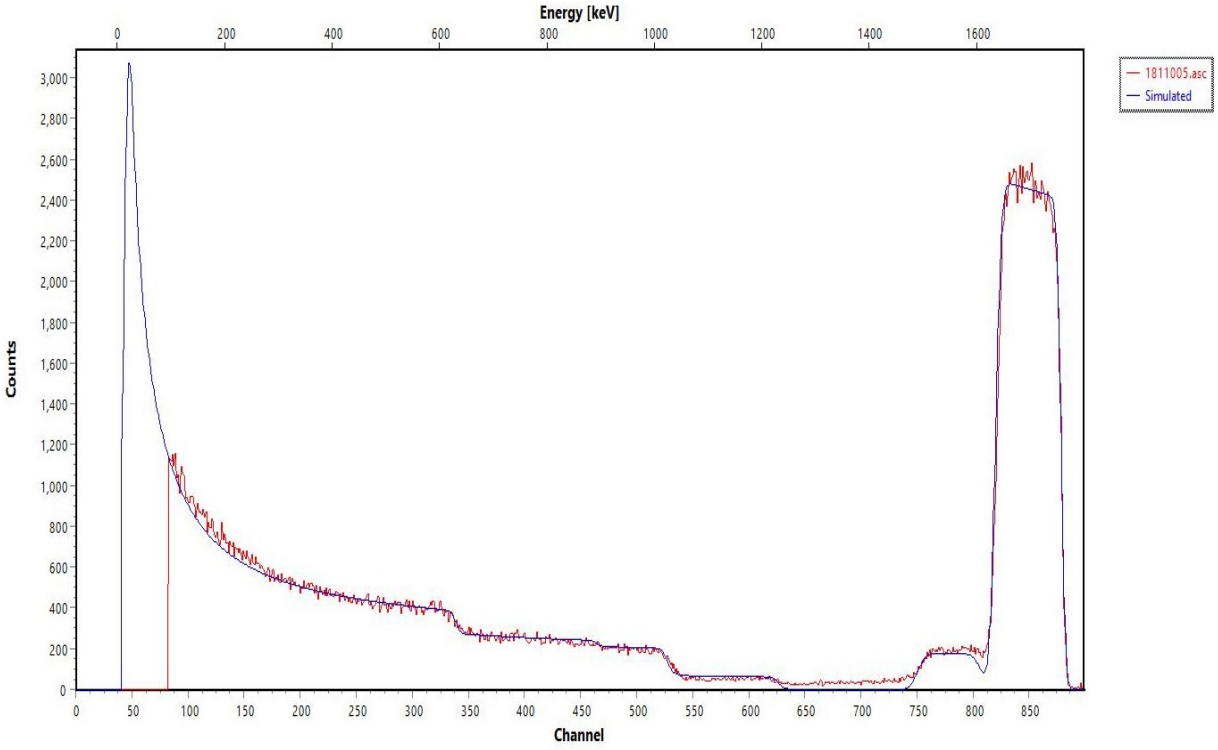

Figure 4.4: RBS spectrum and simulation for GeSb thin film (S4)

Table 4.1 shows the atomic composition and thickness of the film at different laser energies.

Laser Energy (mJ)	Atomic % Ge ±5%	Atomic % Sb ±5%	Atomic Ratio	Thickness (nm)
350	21	79	0.26	295±15
300	17	83	0.20	143±7
200	22	78	0.28	119±6
130	16	84	0.19	119±6
100	15	85	0.17	99±5

Table 4.1: The atomic composition and thickness of films deposited at different laser energies, samples S1 to S5.

Figure 4.5 shows the effect of laser energy on the film thickness. Film thickness (and therefore deposition rate) remains nearly constant as laser energy is increased from 100 to 300 mJ. A sudden increase of deposition rate is noticeable at 350 mJ.

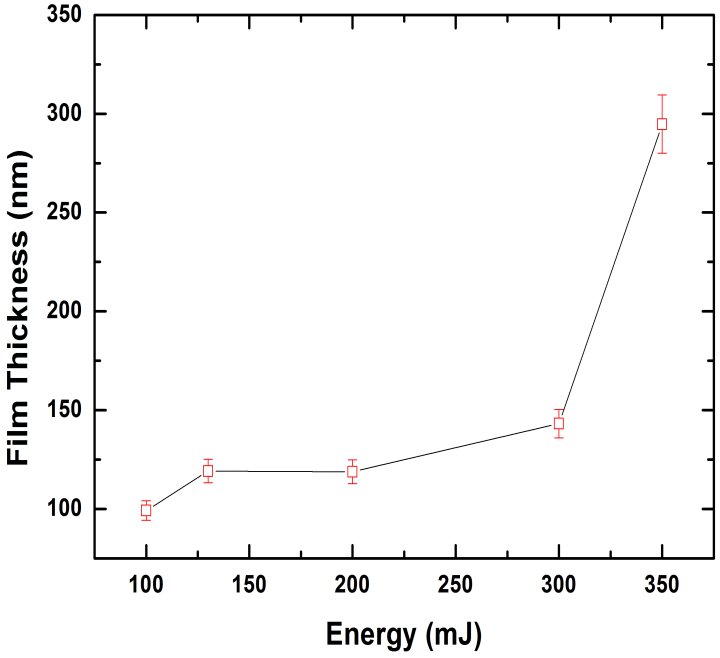

Figure 4.5: The variation of film thickness as function of Laser's energy

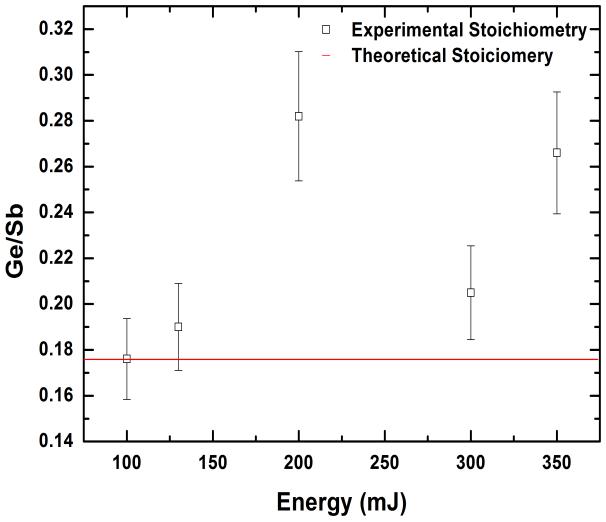

Figure 4.6: The variation of the ratio of Ge/Sb as a function of laser energy

Figure 4.6 shows the Ge/Sb ratio obtained at different laser energies. The theoretical stoichiometry is also shown. The Ge/Sb ratios that are closest to the theoretical value are obtained for low energies, namely 100 and 130 mJ. For higher energies, the values of the Ge/Sb ratio are higher than 0.18 and beyond the 5% experimental uncertainity.

4.2.2 Effect of Deposition Pressure

Five GeSb films were grown at different values of deposition pressure, from vacuum ($\approx 10^{-5}$) up to 10^{-1} mbar of pure Argon gas. For these films, the laser energy was fixed at 200 mJ. The corresponding XRD signals are represented in figure 4.7. None of the samples show any clear diffraction peak indicating that the samples, grown at room temperature, are amorphous.

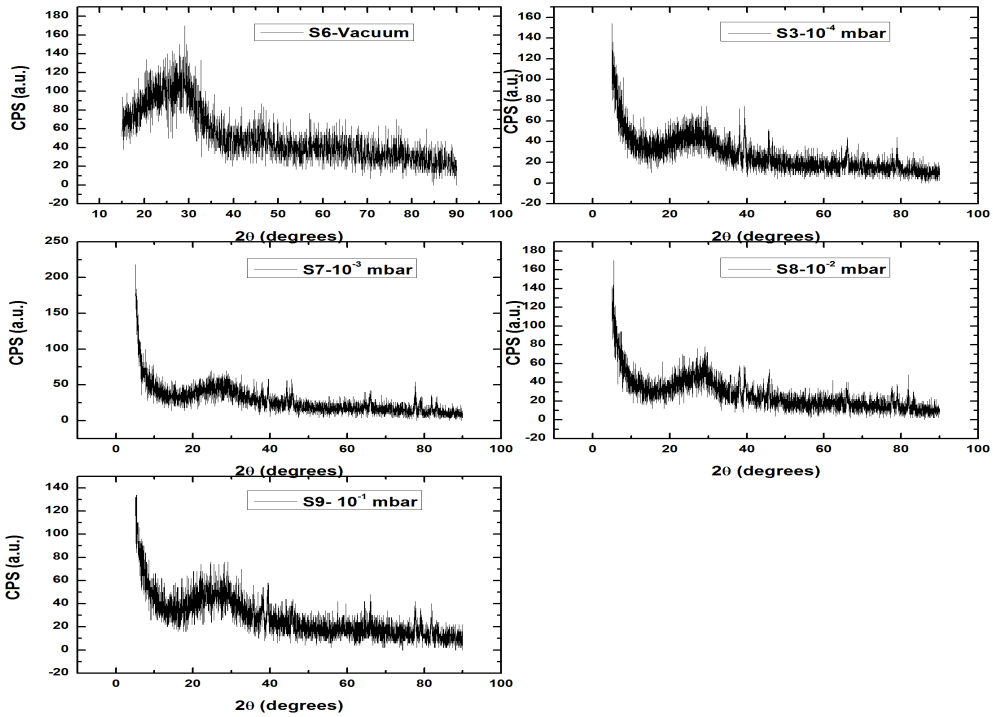

Figure 4.7: XRD spectra of GeSb samples deposited at different pressures

Figure 4.8 shows the SEM images of the films deposited at different Argon pressures. One common feature is that all films show the formation of droplets on their surface. However, the density of droplets appears to vary, and it becomes higher at higher deposition pressure. The change in the surface morphology could be associated wirh the plasma plume dynamics in a certain atmosphere. The plasma plume contains ions, electrons, atoms, molecules and clusters. Their kinetic energy is high because of the high energy of the laser beam. In the case of deposition in vacuum, due to absence of a gas, the particles will arrive to the substrate with high kinetic energy will consequently diffuse on the film surface and smoothen the film. With increasing pressure, the particles in the plume may experience more scattering and collisions which is a reduction of their kinetic energy. Therefore, the film deposited in the Ar atmosphere contains more droplets and clusters than the films deposited in vacuum and as the background Argon pressure increases the surface of the film becomes rougher. The type of the chamber gas can greatly change the surface mobility of the impinging particles, and therefore the change in the particles surface mobility may affect the surface morphology [32].

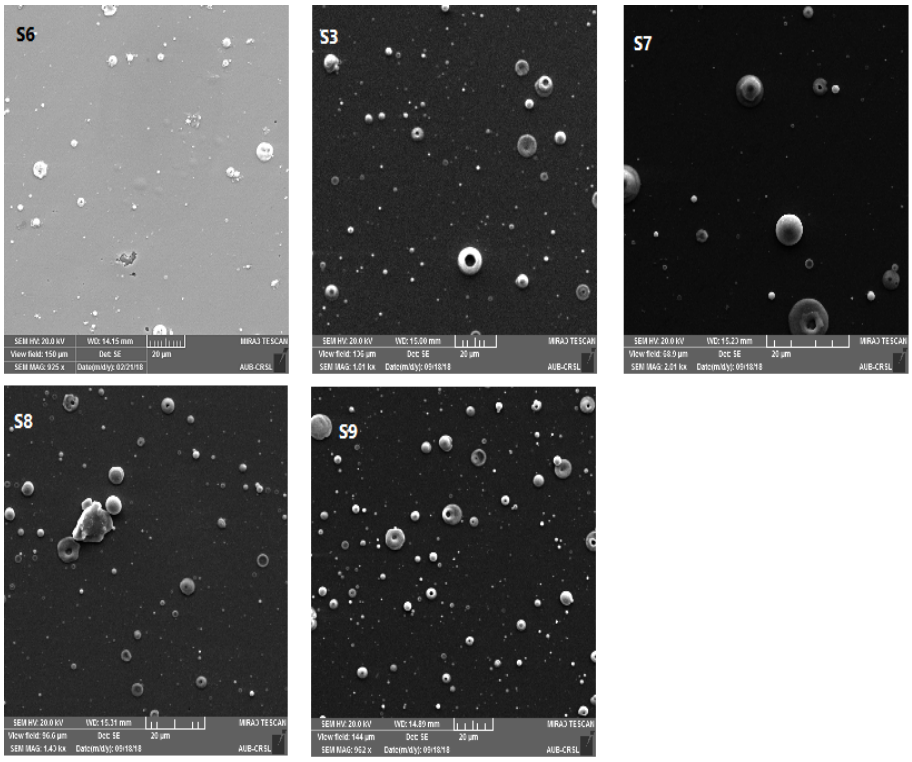

Figure 4.8: SEM images of the GeSb films deposited in vacuum,and at different Argon pressures, 10^{-4}, 10^{-3}, 10^{-2} and 10^{-1}

The effect of the chamber pressure on the film composition and thickness is summarized in table 4.2.

Ar Pressure (mbar)	Atomic % Ge ±5%	Atomic % Sb ±5%	Atomic Ratio	Thickness (nm)
Vacuum	17	83	0.20	99±5
$1.2 * 10^{-4}$	22	78	0.28	119±6
$1.4 * 10^{-3}$	18	82	0.22	119±6
$1.2 * 10^{-2}$	23	77	0.3	183±9
$1.0 * 10^{-1}$	29	71	0.41	141±7

Table 4.2: The atomic composition and thickness of films deposited at different chamber pressure.

The thickness of the films is affected by varying the argon pressure. The plume particles dynamics (kinetic energy, collision and scattering) has an essential role in determining the film thickness, and they are correlated with the mean free path of the ejected particles [33]. The thinnest film was deposited under vacuum. This can be explained as follows. In vacuum, the plume particles move with their original high energy which causes re-sputtering of the previous layer as they reach the substrate. This re-sputtering leads to a thin layer. On the other hand, in the case of argon atmosphere, the particles (ions and atoms) might be slowed down by the Ar atoms thereby limiting re-sputtering and leading to thicker films.

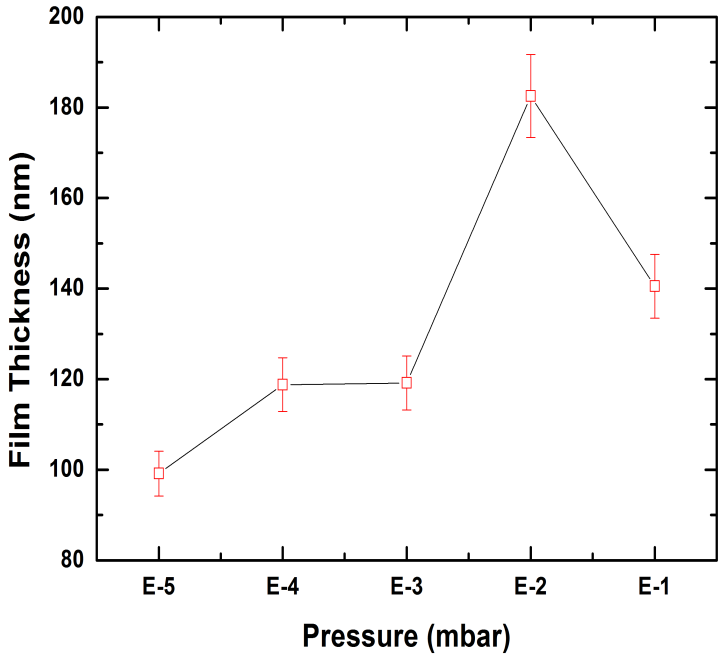

Figure 4.9: The variation of film thickness as function of Argon pressure

Figure 4.9 shows the variation of film thickness with the change in Argon pressure. In PLD process under vacuum deposition condition, re-sputtering from the film surface occurs due to the presence of energetic particles in the plasma plume. It involves re-emission of deposited materials due to ion bombardment. As argon gas pressure increases to 10^{-4} mbar, a reduction of the particle energy is accompanied with a decrease of re-sputtering and a rise in the deposition rate. In contrast, for higher gas pressures, scattering of ablated material out of the deposition path between target and substrate is observed, leading to a decrease in the deposition rate, as seen at 10^{-1} mbar

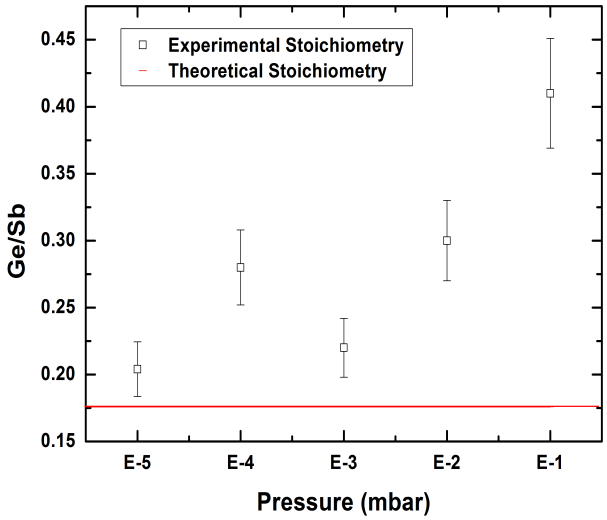

Figure 4.10: The variation of Ge/Sb as a function of Argon Pressure

The Ge/Sb ratio also varies with background pressure as shown in figure 4.10. The atomic ratio of Ge:Sb films prepared under 10^{-3} mbar pressure is very close to the theoretical value whereas there is a significant deviation in the atomic percentage as the argon pressure increases (above 10^{-3} mbar). This phenomenon can be a result of the different scattering behaviour between the Ge and Sb ablated species as the Argon background pressure is increased.

4.2.3 Effect of Deposition Time

The aim of this section is to study the influence of changing deposition time on the prepared films. Two samples are prepared at 1:30 and 3:30 hours. XRD patterns of GeSb deposited at different deposition times do not show any diffraction peak, indicating the amorphous nature of the films.

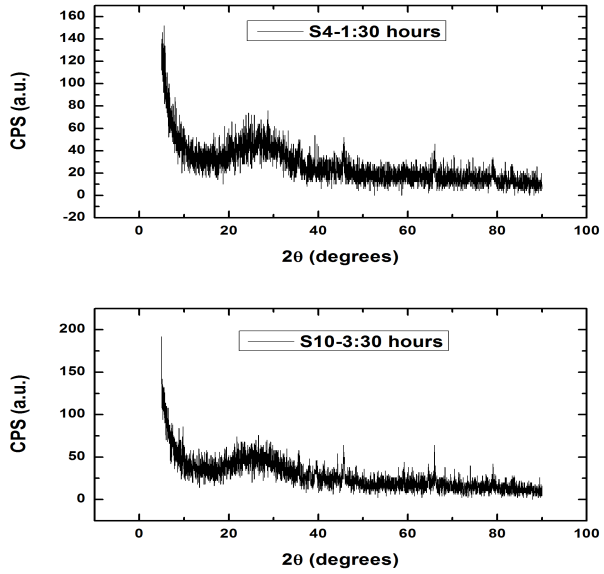

Figure 4.11: XRD spectra of GeSb samples deposited at different deposition times

The SEM images shown in figure 4.12 show that the film deposited for 3:30 hours has lesser amount of droplets than that deposited at 1:30 hours. Hence, the deposition time affects the surface morphology of GeSb thin films; as the deposition time increases the surface of the film becomes smoother.

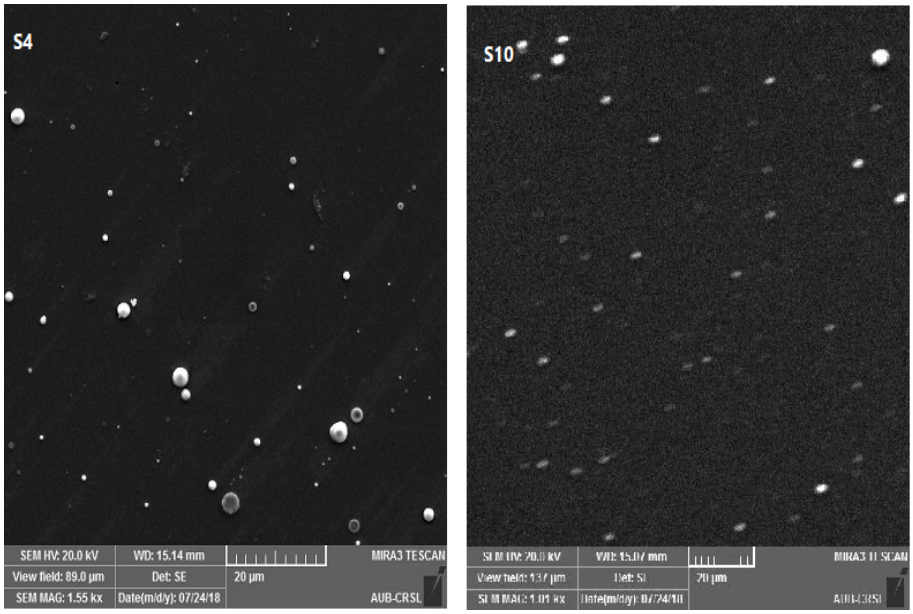

Figure 4.12: SEM images of the GeSb films deposited at different deposition time 1:30 and 3:30 hrs respectively

Film composition and thickness are investigated using RBS technique and the results are summarized in the below table.

Deposition Time (hr)	Atomic % Ge±5%	Atomic % Sb±5%	Thickness (nm)
1:30	17	83	119±6
3:30	17	83	140±7

Table 4.3: The atomic composition and thickness of films deposited at different deposition time.

Table 4.3 shows the results of the two thicknesses of the deposited samples. The film thickness increased slightly from 119 nm to 140 nm as deposition time increases from 1:30 hrs to 3:30 hrs. A much greater increase was expected. One possible explanation of the small increase observed is the deposition of ablated species on the quarts window in the chamber. This would limit the energy of the beam entering the chamber, thus reduces deposition rate.

4.3 Electrical Properties

4.3.1 Effect of Laser Energy

The resistance measurements are carried out on the samples at temperatures between 25°C and 270°C and at a heating rate of 5 K/min. Resistance versus temperature graphs are plotted to determine the amorphous-crystalline transition temperatures (T_c) and its width such plots are shown in figure 4.13 for films deposited at different laser energies. Moreover, the electrical band gap of the samples deposited at different energies are determined from the slope of Ln (R) versus 1000/T (figure 4.14) and the results are listed below in table 4.4. Note that the transition temperature is determined according to the following:

$$T_c = T_a + \frac{transitionwidth}{2} \tag{4.1}$$

where T_a is the temperature at the beginning of the transition

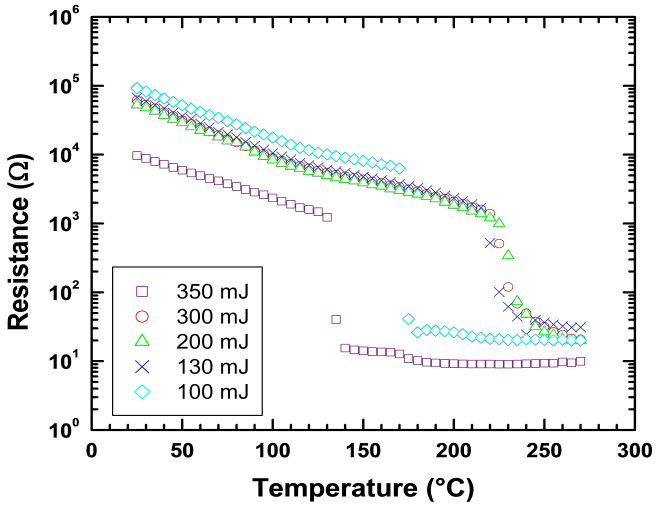

Figure 4.13: Resistance of the deposited GeSb films at different laser energies

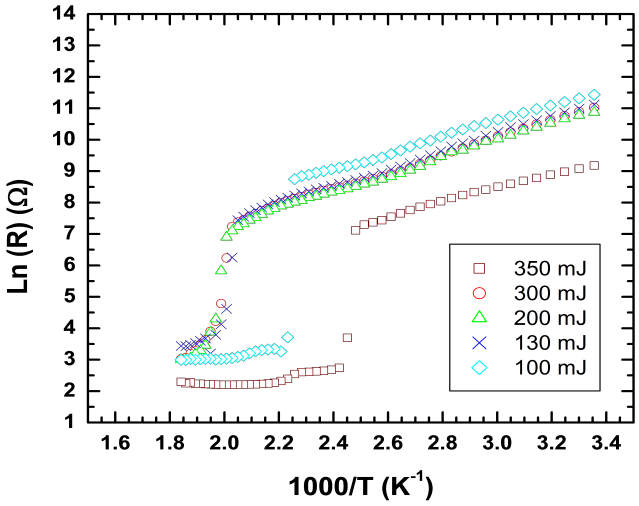

Figure 4.14: Arrhenius plots of ln (R) versus 1000/T for GeSb films deposited under different laser energies.

Samples name	Laser Energy (mJ)	Electrical E_g (eV) ± 0.04	T_c ($^\circ C$)	Transition Width ($^\circ C$)
S1	350	0.39	130	20
S2	300	0.48	220	30
S3	200	0.46	230	20
S4	130	0.47	230	25
S5	100	0.45	175	15

Table 4.4: The crystallization temperature T_c, electrical band gap, and transition width of films deposited at various laser energies.

The results show that the phase transition temperature of the samples is different upon changing the laser energy. The transition temperatures are 130°C, 220°C, 230°C, 230°C and 175°C for the samples from energy 350 mJ to 100 mJ respectively. The fast transition temperature at 350 mJ due to the crystallization that happened in the film deposited at 350 mJ and a higher crystallization temperature around 230°C for GeSb binary materials [18]. The reported transition temperatures at low energies is higher than that at high energy (350 mJ). This was previously shown in a study on the influence of laser energy on $Ge_2Sb_2Te_5$ thin films prepared by pulsed laser deposition [34].

The change in laser energy only affects the electrical band gap of the sample deposited at high energy (350 mJ) where its energy band gap is less than the samples deposited at low energy. All other samples have an energy gap around 0.465 eV except the sample deposited at energy (350 mJ) which has an energy gap of 0.387 eV. This decrease in the energy band gap is due to the crystallization

of the sample at high laser energy.

4.3.2 Effect of Deposition Pressure

The resistance measurements are carried out on samples deposited at different pressures at temperatures between 25°C and 270°C and at a heating rate of 5 K/min. Results are shown in figure 4.15 and figure 4.16 (Arrhenius plots).

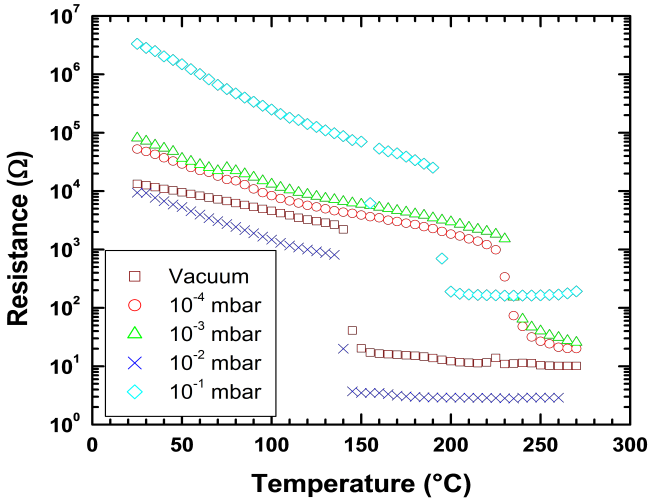

Figure 4.15: Resistance of the deposited GeSb films at different Argon pressure measured with heating rates of 5 K/min

In figure 4.15, the electrical band gap of the samples S6, S3, S7, S8 and S9 are determined from the slope of Ln (R) versus 1000/T and the results are listed in table 4.5. All of the four samples S6, S3, S7 and S8 have energy bands ranges between 0.39 and 0.48 eV. However, S9 sample that is deposited at the highest pressure has 0.69 eV band gap possibly due to the increase in the atomic percentage of Ge atoms.

Samples name	Pressure (mbar)	Electrical E_g (eV) ±0.04	T_c ($°C$)	Transition Width ($°C$)
S6	Vacuum	0.39	145	15
S3	$1.2 * 10^{-4}$	0.46	230	20
S7	$1.4 * 10^{-3}$	0.48	230	25
S8	$1.2 * 10^{-2}$	0.47	140	25
S9	$1.0 * 10^{-1}$	0.69	190	15

Table 4.5: The crystallization temperature T_c, electrical band gap, and transition width of films deposited at various chamber pressure.

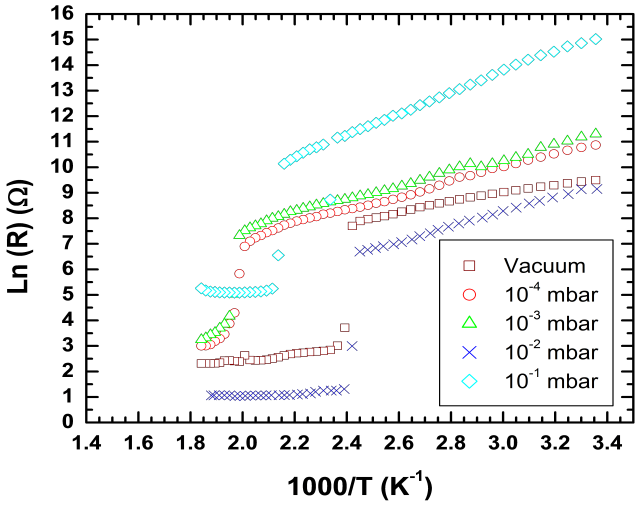

Figure 4.16: Arrhenius plots of ln (R) versus 1000/T for GeSb films deposited under different Argon pressure.

As far as T_c is concerned, samples S3 and S7 show very similar values ($230°C$), significantly higher than the other films. Such difference is most likely correlated to difference in the nanostructure in the layers.

4.3.3 Effect of Time

Figures 4.17 and 4.18 show resistance measurements performed on two samples grown for different times.

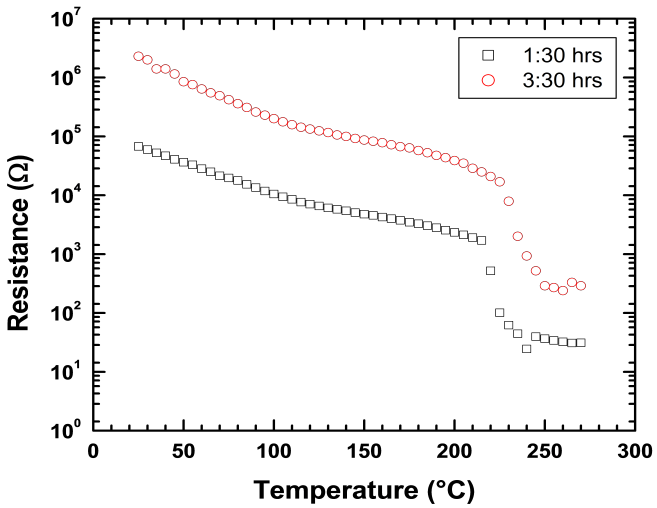

Figure 4.17: Resistance of the deposited GeSb films at different deposition time

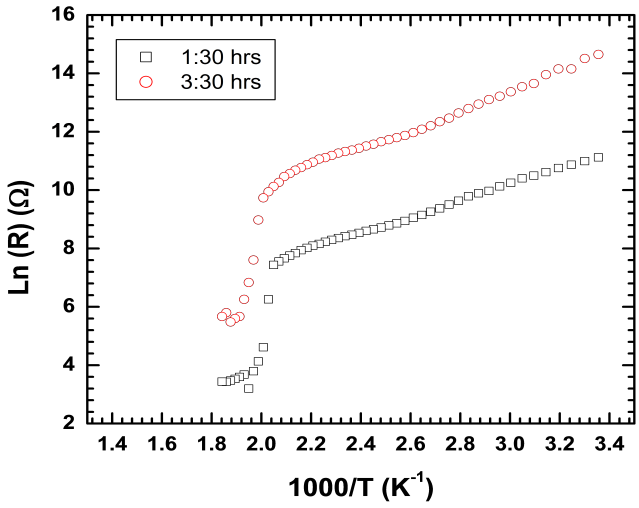

Figure 4.18: Arrhenius plots of ln (R) versus 1000/T for GeSb films deposited under different deposition time.

The results of the electrical measurements are summarized in table 4.6.

Samples name	Deposition Time (hrs)	Electrical E_g (eV)	T_c ($°C$)	Transition Width ($°C$)
S4	1:30	0.47±0.04	220	25
S10	3:30	0.56±0.05	225	20

Table 4.6: The crystallization temperature T_c, electrical band gap, and transition width of films deposited at various deposition time.

Both E_g and T_c are determined to be greater for the film deposited for the longer time. This indicates that deposition time has an effect on the structure of the layers.

4.4 Optical Properties

4.4.1 Effect of Laser Energy

The optical band gap in amorphous semiconductors can be determined using the Tauc relation [35], which is expressed as: $(\alpha h\nu) = B(h\nu - E_g)^r$ Where B is a constant and r is an index which depends on the nature of electronic transition responsible for the optical absorption. Values of r for allowed direct and indirect transitions are 1/2 and 2 respectively. Our results show a linear behavior of $(\alpha h\nu)^{1/2}$, which means an indirect transition from the valence to conduction bands. The corresponding indirect energy band gap can be obtained from the intercept of the resulting straight lines with the energy axis.
Figure 4.19 shows the Tauc plots of the optical absorption spectrum measured at room temperature for GeSb film deposited at different laser energies. The values of the thus-determined optical band gap of the films are reported in table 4.7 and plotted in figure 4.20.

Samples name	Laser's Energy (mJ)	Optical $E_g(eV)$±0.03
S1	350	0.20
S2	300	0.40
S3	200	0.38
S4	130	0.40
S5	100	0.37

Table 4.7: The optical band gap of films deposited at different laser energies.

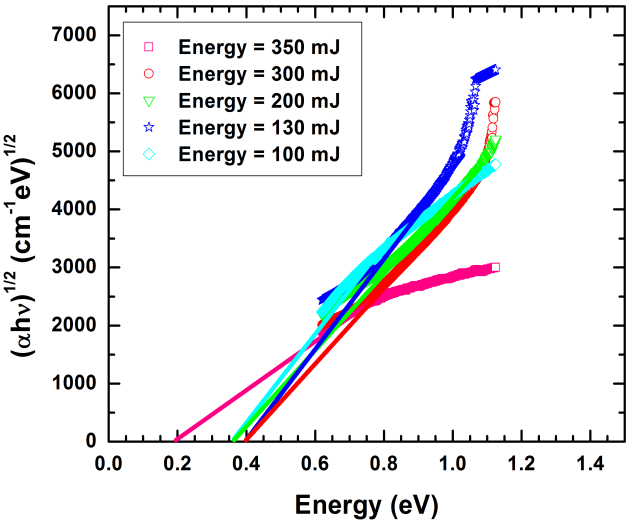

Figure 4.19: Variation of $(\alpha h\nu)^{1/2}$ versus photon energy $(h\nu)$ for the GeSb films deposited under different laser energies.

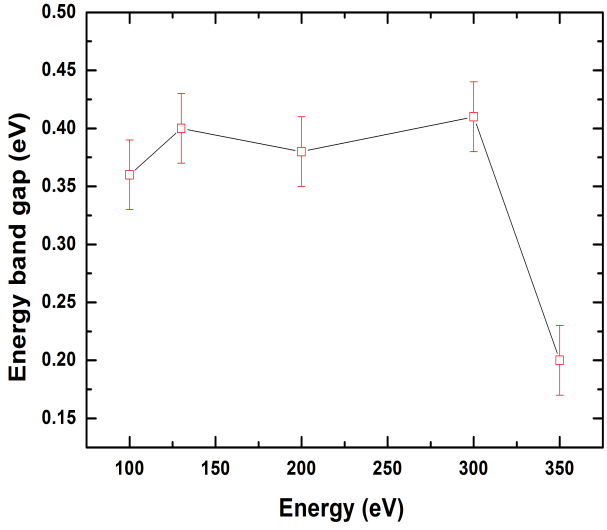

Figure 4.20: Variation of optical energy gap for GeSb Films deposited at different laser energies

The optical band gaps of the samples is in agreement with those of the electrical ones where the energy band gap of samples deposited at 300 mJ till 100 mJ is about 0.4eV. Only S1 sample grown at 350 mJ, shows a smaller energy gap possibles as an effect of crystallization of the film.

4.4.2 Effect of Deposition Pressure

Tauc plots and the deduced optical gap for films grown at different pressures are shown in figures 4.21 and 4.22, respectively. The results are also summarized in table 4.8.

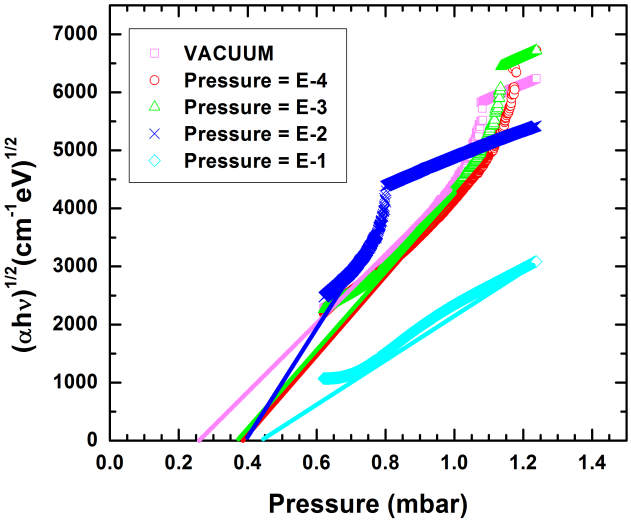

Figure 4.21: Variation of $(\alpha h\nu)^{1/2}$ versus energy $(h\nu)$ for GeSb films deposited at different Argon pressure

Samples name	Pressure (mbar)	Optical $E_g(eV)$ ± 0.03
S6	Vacuum	0.30
S3	$1.2 * 10^{-4}$	0.38
S7	$1.4 * 10^{-3}$	0.36
S8	$1.2 * 10^{-2}$	0.40
S9	$1.0 * 10^{-1}$	0.44

Table 4.8: The optical band gap of films deposited at different chamber pressure.

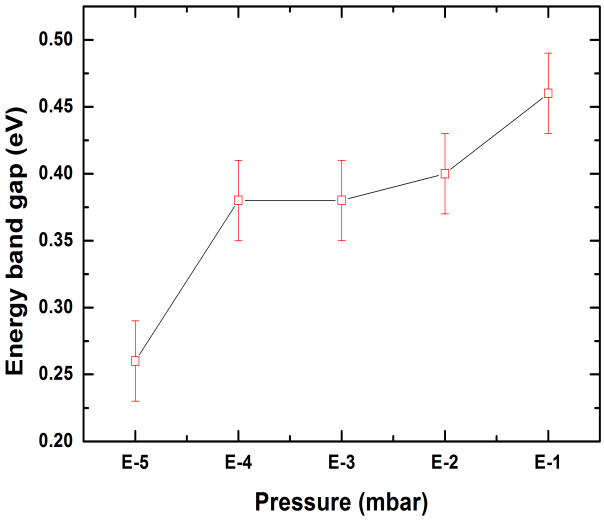

Figure 4.22: Variation of energy gap for GeSb films deposited under different pressures

For the sample deposited under vacuum, the optical gap is close to 0.3 eV, and it increases as deposition pressure is increased from 10^{-4} to 10^{-2} mbar. Further increase in pressure leads to a sharper increase of the band gap, reaching 0.44 eV. These variations of the optical gap are parallel to those of the electrical gap, except that the determined value of the latter is consistently lower than the optical gap. We realize that the optical energy gap is slightly smaller than the electrical one. This is due to the fact that the optical gap is determined from the absorption coefficient by either fitting a function such as that of Tauc, or by selecting arbitrarily an absorptivity that is considered indicative of having reached that band gap. The electrical gap can for example be measured by wavelength-dependent photo-conductivity measurements or by resistance-dependent temperature measurements. The data can be analyzed with similar processes but here not all absorbed photons contribute to the signal, but only those that excite carriers to states where the carriers are mobile. This is mainly relevant in amorphous semiconductors which can have substantial densities of "tail" states, states near the band edge that allow plenty of absorption but little transport, because the states are localized.

4.4.3 Effect of Deposition Time

Tauc plots are shown in figure 4.23 for two samples grown at different deposition time, namely 1:30 and 3:30 hours. The corresponding values of the optical band gap are operated in table 4.9.

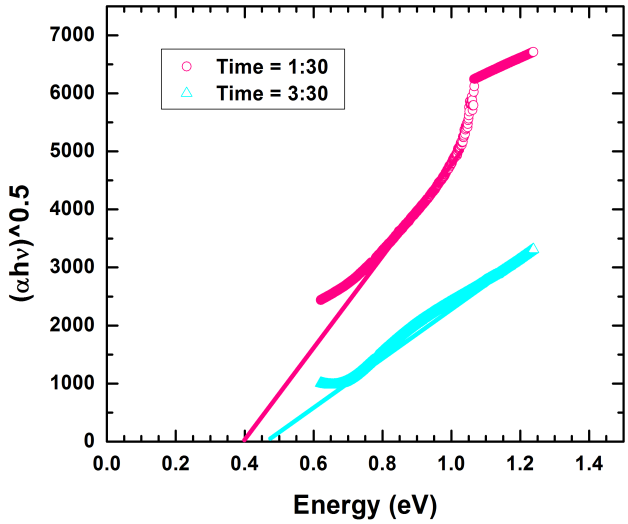

Figure 4.23: Variation of $(\alpha h\nu)^{1/2}$) versus photon energy for GeSb films under different deposition times

Samples name	Deposition Time (hrs)	Optical $E_g(eV)$
S4	1:30	0.40±0.03
S10	3:30	0.47±0.03

Table 4.9: The optical band gap of films deposited at different deposition time.

The energy gap reported for sample S10 (deposited at 3:30 hr) is close to the energy gap previously reported for GeSb thin films. The energy gap of the amorphous GeSb is 0.5eV [20]. Clearly the long deposition time (3:30 hrs) influences the band gap energy.

4.5 Effect of Annealing

The effect of anneain (up to 350°C) on the bonding and physical properties of the films was investigated.

4.5.1 Raman Spectroscopy

The Raman measurements were carried out on the S5 and S4 as-deposited samples and after heating them to 380°C.

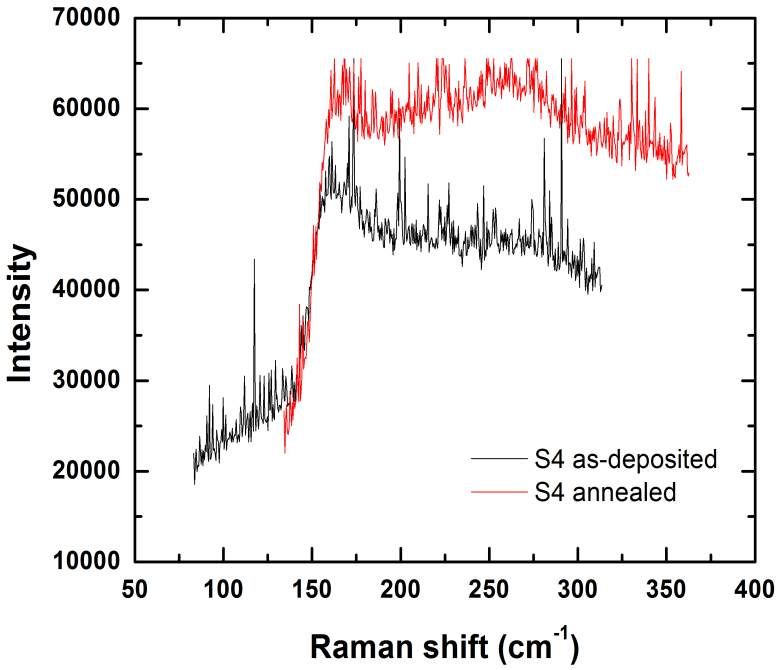

Figure 4.24: Raman spectra for S4 as-deposited and annealed samples

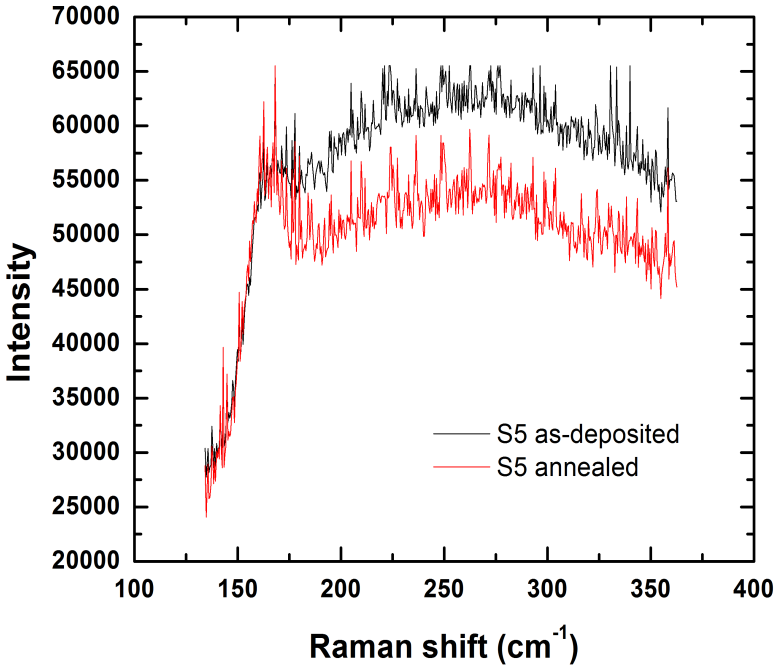

Figure 4.25: Raman spectra for S5 as-deposited and annealed samples

Figures 4.24 and 4.25 show the Raman spectra of the two samples S4 and S5 before and after annealing respectively. A peak for both as-deposited samples is observed at 160 cm^{-1} and 165 cm^{-1} for S4 as-deposited and S5 as-deposited respectively. These peaks correspond to the Sb-Sb bond. A broad peak is also observed in S5 as-deposited between 200 cm^{-1} and 305 cm^{-1}, whereas a small broad peak is observed in S4 as-deposited between 250 cm^{-1} and 290 cm^{-1}. These peaks correspond to the Ge-Ge bond.
The Raman spectra of the annealed samples shown in both Figures are somehow similar to the as-deposited ones. A small peak is observed at approximately 260 cm^{-1} in the thermally annealed samples, which is due to Ge-Ge amorphous bonds. Segregation of Ge is observed, in other paper,at temperature of 420° where under this temperature and above 360° the Ge peak starts to appear slightly [20]. This coincide with our results where a small peak of Ge-Ge starts to appear at 380°.

4.5.2 Optical Properties

Figure 4.26 shows the tauc plot for S5 and S4 annealed samples at (380°C). The extrapolation of the linear part of the graph did not intersect with the abscissa. This implies that after heating the samples, no energy band transition is detected, indicating a metallic behaviour of the film.

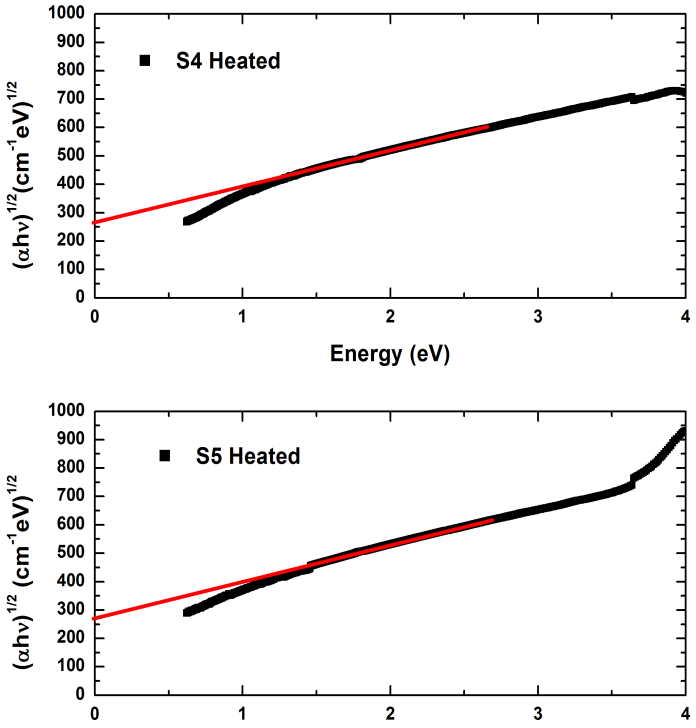

Figure 4.26: Variation of $(\alpha h\nu)^{1/2}$ versus energy for heated GeSb samples

4.5.3 Electrical Properties after Heating and Annealing

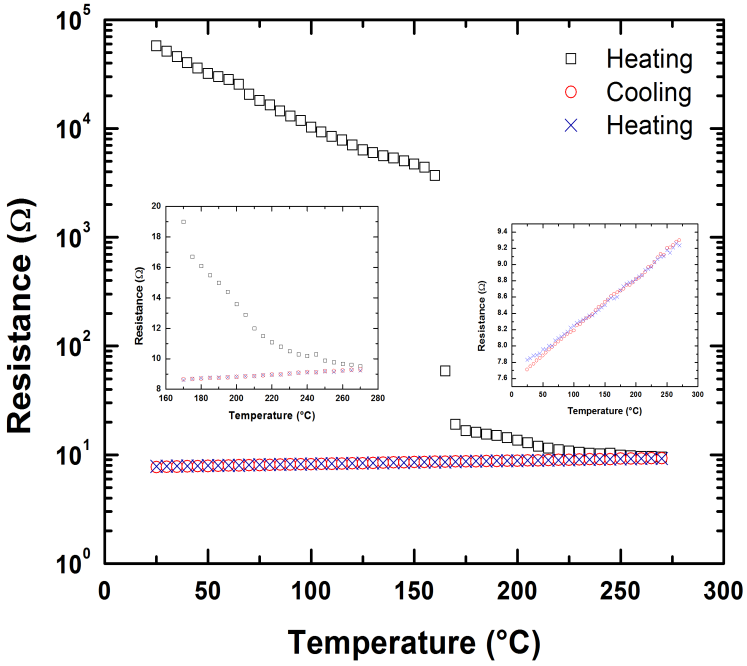

Figure 4.27: Resistance of GeSb during heating and annealing

Figure 4.27 shows the variation of resistance with temperature. After the transition temperature at $170°C$, we can realize that there is a progress in the transition where the resistance is still decreasing with temperature. This region indicates a metastable phase where the film did not yet reach its metallic behaviour. In the cooling phase, the decrease in the temperature is accompanied by a decrease in the resistance whereas, as we reheat the film again the resistance increases proportionally with the temperature indicating the metallic behaviour of GeSb. This can be explained by the additional p electrons as active conductive carriers, significantly attributed to bands near the Fermi level and possibly leading to the metallic behavior of GeSb. Metallic behaviour maybe due to the presence of the fermi-level in the conduction band, a degenerate semiconductor, since the deposited samples are N-type. The N-type semiconductor GeSb is due to the presence of the negative free charge electron from antimony (Sb) material after its bond with germanium (Ge) [20].

Chapter 5

Conclusion

In this work, we investigated the growth of PCM Germanium Antimony thin films on glass (SiO_2) using pulsed laser deposition tecnique. All films were grown at room temperature. Laser energy, deposition pressure, and deposition time were varied and the films were charactarized by: X-Ray Diffraction (XRD), Scanning Electron Microscopy (SEM), Rutherford Back scattering technique (RBS) and Raman spectroscopy. In addition, UV-VIS-NIR spectroscopy was used to determine the optical band gap, whereas sheet resistance measurement as a function of temperature using a two probe method allowed the determination of the transition temperature of the films and their electrical energy gap. It was found that stoichiometric $Ge_{15}Sb_{85}$ amorphous thin film showing clear phase transition can be obtained by growth at room temperature at low laser energy (below 200 mJ) in order to reduce droplet formation. In addition, stoichiometry is conserved when deposition is performed at an Argon background pressure of 10^{-3} and below. Temperature dependant sheet resistance measurement show sharp transitions but the transition temperature depends very much on deposition conditions. Optical and electrical band gap measurements are in agreement with those reported in the literature and preliminary Raman spectroscopy measurements have been carried out to correlate between the properties if the films and its nanostructure. Future work should include an in-depth Raman analysis of the films as well as the investigation of the doping of the films on their pahse change properties.

Appendix A

List of samples

Sample name	Laser Energy (mJ)	Ar Pressure (mbar)	Deposition Time (hours)
S1	350	10^{-4}	1:30
S2	300	10^{-4}	1:30
S3	200	10^{-4}	1:30
S4	130	10^{-4}	1:30
S5	100	10^{-4}	1:30
S6	200	vacuum	1:30
S7	200	10^{-3}	1:30
S8	200	10^{-2}	1:30
S9	200	10^{-1}	1:30
S10	200	10^{-4}	3:30

Bibliography

[1] M. Anbarasu and M. Wuttig, "Understanding the structure and properties of phase change materials for data storage applications," *Journal of the Indian Institute of Science*, vol. 91, no. 2, pp. 259–274, 2012.

[2] M. Wuttig and N. Yamada, "Phase-change materials for rewriteable data storage," *Nature materials*, vol. 6, no. 11, p. 824, 2007.

[3] S. R. Ovshinsky, "Reversible electrical switching phenomena in disordered structures," *Physical Review Letters*, vol. 21, no. 20, p. 1450, 1968.

[4] N. Yamada, E. Ohno, K. Nishiuchi, N. Akahira, and M. Takao, "Rapid-phase transitions of gete-sb2te3 pseudobinary amorphous thin films for an optical disk memory," *Journal of Applied Physics*, vol. 69, no. 5, pp. 2849–2856, 1991.

[5] M. Zhu, *Ti-Sb-Te Phase Change Materials: Component Optimisation, Mechanism and Applications*. Springer, 2017.

[6] H.-S. P. Wong, S. Raoux, S. Kim, J. Liang, J. P. Reifenberg, B. Rajendran, M. Asheghi, and K. E. Goodson, "Phase change memory," *Proceedings of the IEEE*, vol. 98, no. 12, pp. 2201–2227, 2010.

[7] S. Cho, J. Yi, Y. Ha, B. Kuh, C. Lee, J. Park, S. Nam, H. Horii, B. Cho, K. Ryoo, *et al.*, "Highly scalable on-axis confined cell structure for high density pram beyond 256mb," in *Digest of Technical Papers. 2005 Symposium on VLSI Technology, 2005.*, pp. 96–97, IEEE, 2005.

[8] S.-J. Ahn, Y. Hwang, Y. Song, S. Lee, S. Lee, J. Park, C. Jeong, K. Ryoo, J. Shin, Y. Fai, *et al.*, "Highly reliable 50nm contact cell technology for 256mb pram," in *Digest of Technical Papers. 2005 Symposium on VLSI Technology, 2005.*, pp. 98–99, IEEE, 2005.

[9] C.-W. Jeong, S.-J. Ahn, Y.-N. Hwang, Y.-J. Song, J.-H. Oh, S.-Y. Lee, S.-H. Lee, K.-C. Ryoo, J.-H. Park, J.-H. Park, *et al.*, "Highly reliable ring-type contact for high-density phase change memory," *Japanese journal of applied physics*, vol. 45, no. 4S, p. 3233, 2006.

[10] C. Cabral Jr, K. Chen, L. Krusin-Elbaum, and V. Deline, "Irreversible modification of ge 2 sb 2 te 5 phase change material by nanometer-thin ti adhesion layers in a device-compatible stack," *Applied physics letters*, vol. 90, no. 5, p. 051908, 2007.

[11] T. Zhang, Z. Song, F. Wang, B. Liu, S. Feng, and B. Chen, "Advantages of sisb phase-change material and its applications in phase-change memory," *Applied Physics Letters*, vol. 91, no. 22, p. 222102, 2007.

[12] T. Zhang, Z. Song, B. Liu, and S. Feng, "Investigation of environmental friendly te-free sisb material for applications of phase-change memory," *Semiconductor Science and Technology*, vol. 23, no. 5, p. 055010, 2008.

[13] J. Kalb, M. Wuttig, and F. Spaepen, "Calorimetric measurements of structural relaxation and glass transition temperatures in sputtered films of amorphous te alloys used for phase change recording," *Journal of materials research*, vol. 22, no. 3, pp. 748–754, 2007.

[14] G. Eising, *Crystallilzation Phenomena in Germanium Antimony Phase-change Films*. University of Groningen Library][Host], 2013.

[15] D. Krebs, "Electrical transport and switching in phase change materials," *Doktorarbeit, RWTH Aachen*, 2010.

[16] C. Cabral Jr, L. Krusin-Elbaum, J. Bruley, S. Raoux, V. Deline, A. Madan, and T. Pinto, "Direct evidence for abrupt postcrystallization germanium precipitation in thin phase-change films of sb–15 at.% ge," *Applied Physics Letters*, vol. 93, no. 7, p. 071906, 2008.

[17] S. Raoux, C. Cabral Jr, L. Krusin-Elbaum, J. L. Jordan-Sweet, K. Virwani, M. Hitzbleck, M. Salinga, A. Madan, and T. L. Pinto, "Phase transitions in ge–sb phase change materials," *Journal of Applied Physics*, vol. 105, no. 6, p. 064918, 2009.

[18] B. G. Kim, J.-H. Bae, S.-M. Jeong, S.-M. Choi, and H.-L. Lee, "Crystallization properties of ge1-xsbx thin films (x= 0.58–0.88)," *Japanese Journal of Applied Physics*, vol. 50, no. 4R, p. 045805, 2011.

[19] Y. Gu, T. Zhang, Z. Song, Y. Liu, B. Liu, and S. Feng, "Characterization of the properties for phase-change material gesb," *Applied Physics A*, vol. 99, no. 1, pp. 205–209, 2010.

[20] C. Liu, X. Cao, J. Wang, Y. Yuan, J. Su, C. Liu, L. Cheng, X. Zhang, J. Li, and X. Zhang, "Investigation on the optical phase change properties of intrinsic gesb and ti-doped gesb," *Optical Materials Express*, vol. 8, no. 4, pp. 936–947, 2018.

[21] E. R. Meinders, A. V. Mijiritskii, L. Van Pieterson, and M. Wuttig, *Optical Data Storage: Phase-change media and recording*, vol. 4. Springer Science & Business Media, 2006.

[22] M. A. Omar, *Elementary solid state physics: principles and applications*. Pearson Education India, 1975.

[23] S. Kugler, "What is the origin of tail states in amorphous semiconductors?," in *Journal of Physics: Conference Series*, vol. 253, p. 012013, IOP Publishing, 2010.

[24] M. Kastner, D. Adler, and H. Fritzsche, "Valence-alternation model for localized gap states in lone-pair semiconductors," *Physical Review Letters*, vol. 37, no. 22, p. 1504, 1976.

[25] M. H. Cohen, H. Fritzsche, and S. Ovshinsky, "Simple band model for amorphous semiconducting alloys," *Physical Review Letters*, vol. 22, no. 20, p. 1065, 1969.

[26] N. F. Mott and E. A. Davis, *Electronic processes in non-crystalline materials*. OUP Oxford, 2012.

[27] P. Le Comber, "Electrical conduction in amorphous semiconductors," *Science Progress (1933-)*, pp. 105–118, 1979.

[28] B.-S. Lee and S. G. Bishop, "Optical and electrical properties of phase change materials," in *Phase Change Materials*, pp. 175–198, Springer, 2009.

[29] M. Birkholz, *Thin film analysis by X-ray scattering*. John Wiley & Sons, 2006.

[30] P. N. Prasad, "Growth and characterization of nanomaterials," *Nanophotonics. John Wiley & Sons Inc. Published Online: Aug*, vol. 26, 2004.

[31] D. Hoffman, B. Singh, and J. H. Thomas III, *Handbook of vacuum science and technology*. Elsevier, 1997.

[32] D. Norton, C. Park, J. Budai, S. Pennycook, and C. Prouteau, "Plume-induced stress in pulsed-laser deposited ceo 2 films," *Applied physics letters*, vol. 74, no. 15, pp. 2134–2136, 1999.

[33] E. Hasabeldaim, O. Ntwaeaborwa, R. Kroon, D. E. Motaung, E. Coetsee, and H. Swart, "Effect of pld growth atmosphere on the physical properties of zno: Zn thin films," *Optical Materials*, vol. 74, pp. 76–85, 2017.

[34] D. Hu, F. Pan, X. Lu, and J. Zhu, "Influence of laser energy on the crystallization of ge2sb2te5 thin film prepared by pulsed laser deposition," *physica status solidi (a)*, vol. 208, no. 12, pp. 2749–2752, 2011.

[35] J. Tauc, "Optical properties and electronic structure of amorphous ge and si," *Materials Research Bulletin*, vol. 3, no. 1, pp. 37–46, 1968.